Classification, segmentation and correlation of zoned minerals

Tom Sheldrake[1*]; Oliver Higgins[1]**

[1]Department of Earth Sciences, University of Geneva, Rue des Maraîchers 13, 1205 Genève
*corresponding author (thomas.sheldrake@unige.ch) twitter: @NatHazTom
**co-author (oliver.higgins@unige.ch)

THIS IS A NON-PEER REVIEW PREPRINT SUBMITTED TO COMPUTERS AND GEOSCIENCES

Authorship statement: TS designed and wrote the code. TS and OH tested the code and wrote the manuscript.

Highlights:

- New methodology to classify minerals in a thin section, using a finite-mixture model approach.
- Using image processing techniques, chemical zonation within phenocrysts has been segmented and correlated across multiple thin sections
- The approach has been used to classify minerals in thin sections of volcanic rocks, and the to correlate zonation within plagioclase phenocrysts.

Computer code availability

. Name of code: Mineral zonation CSC (Classification, Segmentation and Correlation)
. Developers : Tom Sheldrake
. Contact details : Departments of Earth Sciences, University of Geneva, Rue des Maraîchers 13, Genève 1205, Suisse; e-mail: thomas.sheldrake@unige.ch
. Year first available : 2021
. Hardware required : Mineral zonation CSC was run on a computer with 4 cores (4.0 GHz each) and 16 GB RAM.
. Software required: Mineral zonation CSC was run using RStudio and requires the following packages – *flexmix*, *dplyr*, *plyr*, *raster*, *pheatmap*, *pracma*, *pbapply*, *conicfit*, *viridis*, *imager*, and *apcluster*.
. Program language : the code is written in R v4.0
. Program size : 171.1 Mb
. Details on how to access the source code: the source files of *Mineral zonation CSC* can be downloaded from github : https://github.com/tom-sheldrake/Mineral-zonation-CSC

. Name of code: Mineral Classification
. Developers : Tom Sheldrake
. Contact details: Departments of Earth Sciences, University of Geneva, Rue des Maraîchers 13, Genève 1205, Suisse; e-mail: thomas.sheldrake@unige.ch
. Year first available : 2021
. Hardware required : Mineral Classification was run on a computer with 4 cores (4.0 GHz each) and 16 GB RAM.
. Software required: Mineral Classification was run using RStudio and requires the following packages – *flexmix*, *dplyr*, *plyr*, and *raster*.
. Program language : the code is written in R v4.0
. Program size : 44.3 Mb
. Details on how to access the source code : the source files of *Mineral classification* can be downloaded from github : https://github.com/tom-sheldrake/Mineral-Classification.

Abstract:

Minerals exhibit zoning patterns that can be related to changes in the environment in which they grew. Using statistical methods that have been designed to segment optical images, we have developed a procedure to segment zonation within minerals and correlate these zones between multiple crystals using elemental maps. This allows us to quantify the complexity and variability of chemical zoning between different geological samples. Specifically, we employ a simple linear iterative clustering algorithm, which splits the chemical maps into spatially constrained regions of similar chemistry. The result is a texturally segmented crystal, akin to what would be identified by the human eye. To aid the segmentation and correlation of zones, we also introduce a new method to classify multiple mineral phases within a single thin section. This is based on a finite mixture model approach, which proves very effective in removing mixed pixels that will only introduce noise into the segmentation. We provide an example using the mineral phase plagioclase. Using two contemporaneous samples from an eruptive unit on the island of St. Kitts we show that a volcanic bomb (~10cm) and scoria (~2cm) have similar rim compositions but distinctly different core compositions. Our methodology will enable a statistical characterization of 2D complexity of crystals in a variety of different geo-scientific disciplines. This will allow the genesis of different mineral phases to be characterised and directly compared.

Keywords: geochemistry; SLICAP; magma; volcano; plagioclase; anorthite

1. Introduction

Mineral composition is intrinsically linked to the environment in which it precipitated. Hence, when a mineral phase experiences different physical and chemical conditions during its growth, this generates chemical zoning. Crystal zoning can be imaged using electron spectroscopy (e.g., backscatter electron to measure atomic density; Ginibre et al., 2002) or luminescence (e.g., cathodoluminescence – CL; Hanchar & Miller, 1993; Watt et al., 1997; Lee et al., 2005). Chemical changes can be related to micro-scale variability (e.g., boundary effects; Singer et al., 1995) or macro-scale variability within a geological system (e.g., intensive parameter variation; Ginibre et al., 2007). Hence, identifying and quantifying chemical zonation is an important tool to understand both micro- and macro-scale geological processes.

By visually inspecting crystal zoning throughout a geological sample, individual crystals can be targeted for quantitative analysis to decipher causal processes and associated timescales. Measurements are commonly performed using crystal transects (rim to core), spanning the temporal history of its growth. Transects can be compared between crystals (Wallace & Bergantz, 2002), but this can be complicated by stretching of rim to core profiles due to sample cut effects (Cheng et al., 2017; Probst et al., 2018). Quantified crystals can be used as exemplars for groups of subjectively similar crystals, which is informed by the relative pattern of growth and the number of chemical zones present. Additionally, for particular mineral phases it can be possible to quantitatively calibrate BSE or CL images (e.g., Ginibre et al., 2002) and compare thin section scale 2D variation (Humphreys et al., 2013; Cheng et al., 2017).

Geochemical maps offer an opportunity to quantitatively compare crystal populations. However, no systematic approach exists to quantitatively correlate zoned crystals, introducing uncertainty in the statistical significance of different zoning patterns. The aim of the methodology presented here, is to resolve this issue by developing a semi-autonomous routine to analyse chemical maps and correlate crystal zonation. Our approach revolves around principles used in image segmentation and the concept of superpixels, which are defined as spatially constrained regions of pixels that have a similar composition (Achanta et al., 2012; Zhou, 2015). This approach is suited to mineral phases, which grow radially and exhibit spatially constrained zonation. Groups of superpixels are clustered together based on their average composition, such that the zoning patterns do not necessarily replicate the pixel scale variability in chemical composition. The summary of 2D

zonation is simplified in comparison to other methods that directly cluster the raw pixel data, akin to the textural average subjectively identified by eye (e.g., table 1 in Viccaro et al, 2010).

Our approach allows robust quantitative comparison of the pattern and variability of crystal zonation. For the correlation of segmented zones to be reliable, noisy data must be removed a priori. One example of noisy data are 'mixed pixels', which could be pixels crossing the boundary of two different mineral phases, or within a single crystal that contains cracks, mineral or melt inclusions. Computational mineral grain separation is a well-established field employing a variety of approaches: database querying (Gottlieb et al., 2000), multivariate regression (Willis et al., 2017), multivariate clustering (Wilson & MacRae, 2005; Lanari et al., 2014), and image segmentation methods using superpixels (Maitre et al., 2019). The issue of mixed pixels is commonly approached in post-processing of the results (Lanari et al., 2019; Maitre et al., 2019), rather than integrated within the mineral separation algorithm. Instead, we have designed a new approach that accurately separates components of a thin section, of which mixed pixels represent one component. This is computationally slower (i.e. minutes vs seconds) than more traditional methods, but the results are more accurate with a focus on removing noisy pixels.

Magmatic minerals crystallised in igneous systems commonly exhibit zoning patterns related to changes in the state of the host magma (Bachmann & Dungan, 2002; Zellmer et al., 2003; Costa & Chakraborty, 2004; Humphreys et al., 2006; Pietranik et al., 2006; Ginibre et al., 2007; Shcherbakov et al., 2011; Druit et al., 2012; Cashman & Blundy, 2013; Ubide et al., 2015; Bennett et al., 2019; Cao et al., 2019; Weber et al., 2019; Higgins et al., 2021). This is particularly the case in volcanic samples, which can experience multiple magmatic states during their dynamic journey to the surface. Interpreting these zoning patterns provides insight into the processes occurring prior to eruption. We present our method using thin sections of two volcanic samples collected from the island of St. Kitts in the Eastern Caribbean (**Fig. 1a**). We analyse two contemporaneous samples from one stratigraphic unit, formed during an explosive basaltic eruption. One is a volcanic bomb with long axis ~10cm (SK394C; **Fig. 1c**). The other is a smaller scoriaceous sample with long axis ~2cm (SK394A; **Fig. 1b**). Plagioclase and orthopyroxene phenocrysts are present in both samples, with oxide phases commonly in contact with the orthopyroxene. Amphibole phenocrysts are also present in SK394A. Vesicularity exists in both samples, with larger vesicles in the volcanic bomb (SK394C).

For each sample we prepared a thin section and measured a 1cm x 1cm map at 20μm resolution, using a five-channel WDS detector in a JEOL JXA-8530F Electron Microprobe at the University of Lausanne. The operating conditions were as follows: accelerating voltage of 15 keV, beam current of 15 nA, dwell time of 150 ms, and beam diameter of 5 μm. Our analyses focused on plagioclase that exhibits distinct zoning in both samples. Quantitative analyses were made using transects in individual plagioclase crystals in SK394A, whose chemistry spanned the full variability. Internal standards were used to quantify major chemical components of plagioclase (orthoclase [Si^{4+}, K^{+}], andalusite [Al^{3+}], albite [Na^{+}], and wollastonite [Ca^{2+}]). In both samples the chemical variability of plagioclase is controlled by the relative composition of the Ca^{2+} (anorthite) and Na^{+} (albite) end-members (**Supplementary Fig. 1**). Thus, in our analysis we use the counts of these two elements to segment and cluster crystal zonation.

2. Proposed method

The methodology outlined below has been developed to segment individual crystals and correlate zonation across crystals in multiple thin-sections. Our approach is based on three fundamental steps:

1) Classification of the phenocrysts to be studied;
2) Segmentation of textural [spatial-chemical] zones in individual crystals;
3) Correlation of all segmented zones using a geochemical distance metric.

The data required for the first two steps is the raw intensity (integer counts) for the chemical elements of interest. For example, elemental maps of intensity can be measured by wavelength-dispersive spectroscopy (WDS) or energy-dispersive X-ray spectrometry (EDS) using an Electron microprobe (EMPA) or a Scanning Electron Microscope (SEM). Alternatively, a measure of intensity that varies systematically with specific chemical elements could be used (e.g. BSE and anorthite; Ginibre et al., 2002). For the third step, if analytical conditions do not vary between samples the measure of intensity can be directly compared. Without identical conditions, this step will require quantitative standardisation (e.g., converting intensity to wt. %) using a calibration curve for each sample, for the chemical elements of interest. This ensures different samples are directly comparable. Alternatively, a pre-calibrated phase map (e.g., XMapTools; Lanari et al., 2014, 2019) could be used to segment and correlate zonation.

67

68 2.1 Classification

69 We classify the different mineral phases that are present using a two-dimensional finite Gaussian
70 mixture model. This approach excels at identifying mixed pixels (see discussion). It is based on the
71 principle that for different minerals, elements that are present as network-modifying cations (e.g.,
72 Ca^{2+}, Mg^{2+}, K^{+}) occur in different proportions with respect to elements that are present as network-
73 forming cations (e.g., Si^{4+}, Al^{3+}). Hence, transforming the raw data according to the following
74 equations (**Eq. 1-2**) generates two-dimensional Gaussian distributions that characterises each
75 mineral phase present. Depending on the combination of network-modifying cations (NMC) and
76 network-forming cations (NFC) that are chosen, the E-M algorithm will separate mineral phases
77 into different latent classes (i.e. clusters). To classify the chemical data into a series of latent classes
78 we use the *Flexmix* package in R (Leisch, 2004), which uses an expectation-maximisation algorithm
79 to implement the discrete mixture model.

80

81 $$X = 2 \cdot NFC + 1 \cdot NMC \quad \textbf{(1)}$$

82

83 $$Y = 1 \cdot NFC + 2 \cdot NMC \quad \textbf{(2)}$$

84

85 For two elements multiple minerals may belong to the same latent class. This may happen because
86 two phases have similar amounts of both the NMC and NFC (e.g., Al and Ca in orthopyroxene and
87 oxides in **Fig. 2a-c**). Alternatively, if minerals share similar covariance matrices (i.e. two elements
88 vary in similar proportions) they may also be allocated to the same latent class (e.g., amphibole and
89 plagioclase in **Fig. 2a-c**). In this case, multiple minerals are allocated to the same latent class
90 because the EM algorithm has converged to a local maximum. If the EM algorithm had converged to
91 the global maximum it would separate amphibole and plagioclase in **Fig. 2b**. The density of points
92 belonging to these two phases is clearly distinguishable. However, because the samples contain
93 mostly matrix (**Fig. 1b-c**), the majority of pixels contain multiple mineral phases and so
94 convergence to a global maximum is difficult.

95

96 To overcome the issues of multiple phases belonging to the same latent class, we run the EM
97 algorithm for different NMC-NFC combinations. The element choice should be informed by an
98 understanding of the sample (e.g., predominance of mafic vs. felsic phases). For each combination
99 of elements we search for the same number of latent class components, although the EM algorithm
00 may converge to a smaller (and thus different) number of clusters. The number of latent class

components is informed by optical microscopy and analysis of the elemental maps. It should be equal to or larger than the number of individual components observed (e.g., mineral phases, matrix, vesicles).

By running the EM algorithm for different NMC-NFC combinations we overcome the problem of local convergence. For example, whilst Al-Ca doesn't distinguish between orthopyroxene and oxides (**Fig. 2a-c**), because Si is found in orthopyroxene but not oxides, Si-Ca does distinguish these two phases (**Fig. 2d-f**). Furthermore, whilst Al-Ca doesn't distinguish between plagioclase and amphibole (**Fig. 2a-c**), it is possible with Si-Ca (**Fig. 2d-f**). This is because in plagioclase Al and Ca have positive correlation, whereas Si and Ca have negative correlation (**Supplementary Fig. 1**). Thus, for Si and Ca the covariance matrix for transformed parameters is different for plagioclase and amphibole.

Using just three elements (Si-Ca & Al-Ca) we can distinguish all five discrete components in SK394A by assessing the pairwise combinations of clusters (**Table 1**). Nonetheless, three elements is not sufficient to distinguish all mixed pixels. For example, the plagioclase phenocryst at the bottom left of SK394A contains mixed pixels due to the presence of cracks and inclusions (**Fig. 1b**). Using only Si-Ca and Al-Ca, however, these cracks and voids are composed of a mixture of components whose composition is most similar to amphibole. To resolve this we increase the number of possible NMC-NFC combinations. Resultantly, the number of unique combinations of NMC-NFC clusters increases (**Table 2; Supplementary Fig. 2**).

To assess which unique combinations represent phenocryst phases we identify those that have at least one pixel that is entirely surrounded by pixels of the same unique combination. The assumption here is that in a 3x3 grid, if all pixels have the same unique combination of clusters the central pixel cannot be a mixed pixel [*central pixel assumption*]. As we increase the number of possible combinations of NMC and NFC, mixed pixels will be distinguished from phenocryst pixels and less likely to satisfy the central pixel assumption. Thus, the results are more likely to converge to the true solution and mixed pixels will be removed. However, elements in low concentration in all components and close to the instrumental detection limit (E.g. Ti, Cr, Mn) will likely introduce noise into the phenocryst phases and the results will not converge to the true solution (**Supplementary Fig. 3**). There is a computational cost to the increased number of NMC-NFC combinations. For a single map (500 x 500 pixels) the phase classification algorithm took 154.4 seconds to process the 11 combinations in **Table 2**, using a 4GHz i7 processor with 16GB RAM.

In some cases the finite mixture model will not converge for particular combinations of elements (**Supplementary Table 1**). In these scenarios care must be taken when choosing the final combinations of elements to classify phases. Increasing the number of iterations that the EM algorithm can run for, or repeating it for different number of latent class components (Leisch, 2004), may produce convergence. Such an approach could also aid convergence to a global maximum in examples where not all phases have been properly classified (**Fig. 2b**). Such changes, however, would require manual editing of our code.

In our example we use 11 combinations of elements to classify the mineral phases in our thin sections (**Table 2; Supplementary Fig. 2**). After performing the central pixel assumption 8 groups remain, of which 3 represent mixed pixels, which we classify as matrix (**Supplementary Fig. 4**). SEM imaging of the matrix reveals clinopyroxene microcrystals, not present as a phenocryst phase. It is possible that small clinopyroxene crystals form a chemically discrete group within the matrix and dominate one of the 3 groups of mixed pixels. To generate phase maps (e.g. **Figure 1**), the user must allocate each of these unique clusters to a mineral phase, matrix, or vesicles, based on optical microscopy and the chemical maps. It is possible for one mineral phase to be represented by two groups, especially when the data is clearly separated into multiple discrete solid solution members (e.g., albite and anorthite in plagioclase). The final phase maps are presented in **Figure 1** for SK394A and SK394C.

2.2 Segmentation

Once individual crystals have been classified, we use a segmentation algorithm combining a simple linear iterative clustering (SLIC) and an affinity propagation (AP) algorithm (Frey & Ducek, 2007; Achanta et al., 2012; Zhou, 2015). The SLIC algorithm was originally developed to perform image segmentation on optical images, where pixel composition is represented in a colour space such as CIELAB. The principle of the SLIC method is to identify spatially constrained regions of multiple pixels that share similar characteristics. Each one of these regions is known as a superpixel.

Our segmentation algorithm is performed iteratively on each crystal, which is extracted as a polygon from the phase map. We choose plagioclase due to its presence and clear chemical zonation in both samples. In this example, we take all crystals that have an area that is larger than 81 pixels (**Fig. 1b-c**). We choose this area as it is equivalent to a 3x3 grid of superpixels, where the

centroids are initiated every 3 pixels (see explanation below). For each crystal we extract a rectangular matrix with pixels that belong to one of the following two masks:

- Mask 1: Pixels that lie outside the crystal boundary or pixels that do not represent the mineral phase being analysed.
- Mask 2: Pixels that lie within the crystal boundary and represent the mineral phase.

For all pixels within mask 2 we normalise the measured chemical intensities between zero and one. For all other pixels belonging to mask 1 we set their value to -99 (**Fig. 3**).

SLIC is an iterative algorithm where the centroid of each superpixel is updated repeatedly until convergence is achieved. In our case, the centroid is calculated as the median value of the spatial coordinates and chemical intensities of all pixels with the same superpixel label (l). To initiate the algorithm, centroids are positioned in a regularly spaced grid within the rectangular matrix (**Fig. 4a**). The spacing of the centroids is determined by the parameter *S*, which represents the numbers of pixels between each centroid. The user can choose the value of the parameter *S*, but the default value works well for crystals of different size and shape, and calculated using the following equation:

$$S = 2^{log_{10}[nr \cdot nc]-1} \quad \textbf{(3)}$$

where *nr* is the width and *nc* is the height of the rectangular matrix for the respective crystal. The value of S is rounded to the nearest integer, and the minimum value can be 3.

To ensure convergence and that superpixels are not seeded on noisy pixels, we move the centroids to the lowest average gradient position in all chemical intensities within a 3 x 3 grid (**Fig. 4b**). Additionally, to aid segmentation we force all mask 1 pixels to have a gradient value of -99. All initial centroids that lie on a boundary between pixels belonging to masks 1 and 2 will thus be forced to initiate within the crystal (e.g., i in **Fig. 4b**). Finally, we remove duplicate centroids, which will be more likely to occur in smaller crystals.

Once centroids have been initiated the algorithm is run iteratively. For each iteration, within a $1.5S \times 1.5S$ grid around each centroid, the algorithm calculates a spatial-chemical distance between each pixel and the respective centroid (**Eq. 4**), in which M is used to weight the relative importance

of spatial proximity (**Eq. 5**) versus chemical similarity (**Eq. 6**), where *x* and *y* are the coordinates of the pixel, and *C* represents the concentration for all chosen elements.

$$D = \sqrt{{d_c}^2 + M^2 \cdot (d_s/S)^2} \qquad \textbf{(4)}$$

$$d_s = \sqrt{(x_k - x_i)^2 + (y_k - y_i)^2} \qquad \textbf{(5)}$$

$$d_c = \sqrt{(C_k - C_i)^2} \qquad \textbf{(6)}$$

The user can choose the value of *M*, but the default value works well for crystals of different size and shape (**Eq. 7**), given that chemical intensities are normalised between 0 and 1. By using the finite mixture model to classify mineral phases we are confident this range represents the true chemical variability in each crystal. The inclusion of additional noisy pixels at this stage would reduce the efficacy of the segmentation. However, as a safeguard we describe below an additional step to further reduce the influence of noisy pixels on the results of the segmentation.

$$M = 2S/(nr + nc) \qquad \textbf{(7)}$$

For an individual pixel, when the value of D is smaller than the value in the previous iteration, its label is updated to the index of the superpixel centroid around which the algorithm is currently searching. The algorithm is iteratively repeated 10 times (**Fig. 5a**), sufficient for convergence in SLIC algorithms (Achanta et al., 2012). The user can modify the maximum number of iterations. Finally two post-processing steps are performed. The first removes single pixels whose label is not identical to at least one other adjacent pixel in either the X or Y dimensions. The second step combines duplicate labels that may have converged to the same centroid. Each label is represented by a single centroid (**Fig. 5b**), although it is possible for one superpixel to be split across the image (**Fig. 5c**).

Once an image has been segmented into superpixels, similar superpixels are grouped together. The approach we use is based on the SLICAP algorithm (Zhou, 2015), which uses an affinity propagation (AP) algorithm (Frey & Dueck, 2007). The advantage of the AP algorithm is that it does not require the user to specify the number of clusters. To perform this step we use the *APCluster* package in the R language (Bodenhofer et al., 2011).

Using the AP algorithm, we compare the mean value for all chemical elements of each pairwise combination of superpixel centroids (C_i, C_k), and calculate a negative similarity matrix using the following equation:

$$s_{i,k} \sim \sum -(C_i - C_k)^2 \quad \textbf{(8).}$$

This similarity matrix forms the basis for a series of transformations. Prior to these transformations, however, is the only semi-subjective step of the AP algorithm, which is to define the diagonal values of the similarity matrix. Based on **Eq. 8**, the diagonal values will be zero, which will encourage the AP algorithm to converge to the maximum number of clusters. To avoid over-fitting the number of clusters the diagonal values can be set to a value between the minimum of the non-infinite values in the similarity matrix and zero. We set the diagonal values of the similarity matrix to equal a percentile value of the distribution of non-infinite values. To reduce the influence of pixels that do not belong to the crystal (e.g., cracks) we set all pixels in masks 1 to NA. We also remove from the similarity matrix superpixels that contain > 90% pixels belonging to mask 1. This ensures that noisy pixels belonging to mask 2 (which will make up < 10% of a superpixel) do not bias the AP algorithm. The prevalence of superpixels containing noisy pixels will depend on how mineral phases were classified. Using our approach we observe very few noisy superpixels in our results.

The sensitivity of the results of the AP algorithm to the percentile value (q) will depend upon the aspect ratio and size of the crystal (**Supplementary Fig. 5**). Consequently, we estimate q using the following equation,

$$q = exp^{-q1-q2+q3} \quad \textbf{(9),}$$

where $q1$ is calculated as the ratio of the long and short axes of the ellipse,

$$q1 = X_{long}/X_{short} \quad \textbf{(10),}$$

$q2$ is the area of the large phenocryst (A_{max}) relative to the area of the current phenocryst (A_n),

$$q2 = \ln(A_{max}/A_n) \quad \textbf{(11),}$$

and $q3$ is a constant that can be changed to set the maximum (q_{max}) value of q,

$$q3 = \ln(q_{max} + q1_{min} + q2_{min}) \quad \textbf{(12),}$$

where $q1_{min}$ and $q2_{min}$ both equal 1. In our example we set the value of $q3$ to 1, such that the q_{max} equals 0.05. A final post-processing step is performed where each of the pixels is allocated to one of the clusters identified by the AP algorithm, and all pixels belonging to mask 1 are set to NA. Pixels belonging to superpixels that contain more than 90% pixels belonging to mask 1 are set to NA, but any individual pixels within this group that belong to mask 2 are attributed to the AP cluster value of neighbouring pixels. The result is a single segmented crystal that is texturally correct (**Fig. 6**), but not yet directly comparable to zonation in other samples and crystals.

2.3 Correlation

Once all crystals have been segmented we compare the chemical composition of each zone, using the elements used to segment the crystals. Rather than compare the average composition of each zone, we compare the chemical variability in each zone. To do this we compare the mean distance (d_{mean}) in the cumulative probability distribution for a single chemical parameter (**Fig. 7**). This allows us to compare the shape of the distribution, as well as the absolute values.

When using multiple elements there are two approaches: (1) calculate d_{mean} for each element separately and then calculate the average d_{mean} for all elements; or (2) convert the data into a single chemical parameter (e.g. ratio) and calculate a single mean distance. Given the solid solution zonation in plagioclase between albite (Na) and anorthite (Ca), it is reasonable to calculate d_{mean} for the ratio of these two end members.

As we stated earlier, for samples measured using the same analytical conditions the user may directly compare raw elemental intensities. Otherwise, standardisation to a quantified unit such as weight percent (wt. %) or atoms per formula unit (apfu) is required. To quantify an elemental map a series of standardised analytical points need to be measured. Ideally, these analyses should be made during the same analytical session in which the elemental map was measured. This ensures that the reference frame of the elemental map and analytical points are identical, assisting accurate calibration (e.g., Lanari et al., 2014).

To correlate the segmented zones in our example we calibrate Ca and Na counts in each sample for their respective atoms per formula unit (apfu) (**Supplementary Fig. 6; Supplementary Table 2**), which we in turn use to calculate the approximate anorthite content of the plagioclase in mol. % using the following equation,

$$An = 100 \cdot \left(\frac{Ca^{2+}}{Ca^{2+}+Na^{2+}}\right) \qquad \textbf{(13).}$$

We compare the cumulative probability distribution of anorthite for each zone, across the complete range of anorthite in the two samples, and calculate d_{mean}. We plot the results as a distance matrix and, using hierarchical clustering, identify groups of geochemically similar zones (**Fig. 7-8**). We define these as zoning groups, which are correlated across crystals and samples, forming the chemical building blocks of each crystal.

3. Results & Discussion

The segmentation algorithm splits each phenocryst into a number of different zoning groups based on chemical composition. We analysed 29 and 28 phenocrysts for SK394A and SK394C respectively (**Fig. 9a**) of which all crystals contained 1-3 distinct zoning groups per crystal (**Fig. 9b**). Across both samples we identified 90 (48 + 42) distinct zones in total, which correspond with anorthite composition (**Fig. 9c,d**).

A key aspect of the proposed method is the distance matrix (**Fig. 7)**, which permits quantitative comparison of zoning chemistry. The number of final zoning groups is guided by a qualitative analysis of the distance matrix (**Fig. 7c**), where pairwise combinations of zones with similar d_{mean} are combined. It can be also aided by scoring metrics such as the c-index (**Fig. 7b**; Hubert & Schultz, 1976), which compares within-cluster pairwise distances and within-sample pairwise distances. As the value of the c-index decreases, the number of zoning groups is defined as better describing the data. This suggests the best number of zoning groups is 25 (**Fig. 7b**). This is clearly an over-fitting resulting from the hierarchical structure of the distance matrix. Hence, we base our assessment of the number of groups on identifying the first major plateau in the c-index score.

Choosing six zoning groups ensures crystals that are segmented into multiple zones (**Fig. 9a-b**) also contain multiple zoning groups (**Fig. 8a-b**). Choosing five zoning groups will result in some crystals segmented into multiple zones containing only one zoning group (**Supplementary Fig. 7**), as the

red and yellow zoning groups in **Figure 7c** would be combined. At this stage we observe the success of the algorithms, as fragments from the same crystal are attributed to identical zoning groups.

Irrespective of whether we choose five or six zoning groups, the results can be interpreted in a similar way. All zoned crystals exhibit a rim composition represented by the yellow or red zoning group (**Fig. 8a-b**). The presence of this common rim in both samples supports their contemporaneous nature, being erupted in the same magma. The majority of crystals in both samples are normally zoned, although a few crystals are reversely zoned. Most core compositions belong to light blue zoning group, which is present in both samples and represents the majority of normally zoned crystals (**Fig. 8a-b**). A second pink zoning group, is also present in both samples (**Fig. 8a-b**). It has the lowest An# compositional range (**Fig. 8c**) and is most common as a core, in what are therefore reversely zoned crystals. A third green zoning group represents cores that are only present in the scoriacious sample (**Fig. 8a**). This group of cores has a distinctly high An# compositional range (**Fig. 8c**), indicating crystals that are sourced from a deeper, hotter and more volatile-rich portion of the magmatic system (Sisson & Grove, 1993; Melekhova et al., 2017). Finally, a dark blue zoning group that mantles one of these high-An cores in SK394A, is also present in one fragmented crystal in SK394C that displays patchy zonation.

The maximum number of zones identified within an individual crystal will depend on two main factors: (i) the spatial resolution of the chemical map versus crystal size; and (ii) the average superpixel size, which is a function of the parameter S. The choice of analytical conditions will be determined by the research question that is being investigated. However, given that the minimum value of S can be 3, we suggest that the optimum resolution be set at approximately 1/3 of the smallest feature targeted for segmentation. At these highest resolutions, the image will likely be segmented into more superpixels than necessary. However, whilst this may be computationally inefficient, it will not lead to over-segmentation, which will be limited by both the affinity propagation and hierarchical clustering that follows. For example, if we considered the results in **Figure 9a-b** to be over-segmented, by choosing only five instead of six zoning groups, the complexity in the segmentation is reduced in the correlated crystals (**Supplementary Figure 7**). Finally, the affinity propagation can be optimised by the parameter *q3* (**Eq. 12**) to alter the complexity of the zoning that is segmented.

To this point we have focussed solely on spatial resolution. Chemical precision, however, also influences the efficacy of both the phase classification and segmentation. The chemical precision required will be determined by the mineral phases and the chemistry of zonation (e.g., major vs trace). Ultimately, a judgement will be required between spatial resolution, chemical precision and mapping extent. For example, as we were interested in mapping a large area ($1cm^2$) with medium resolution (20μm) we decided that the WDS detector on an EPMA would provide optimum chemical precision for classification and segmentation.

In porphyritic rocks, such as the samples presented here, the matrix can represent a large proportion of the total mapped area. Consequently, unless the spatial resolution of the imaging method is extremely high (~a few μm) the resulting image will be dominated by a mixed signal. We can observe this effect by comparing the results of our new approach for classifying mineral phases with unsupervised and supervised k-means clustering. The results show our proposed method is most compatible with what we observe under a petrographic microscope, including the distribution and abundance of cracks, inclusions and crystal shape.

K-means clustering is an iterative algorithm that separates data into distinct clusters, by classifying each multivariate data point to the cluster with the nearest mean value. In the unsupervised approach only the number of cluster centres is chosen, whereas in the supervised approach the value of each centre is initiated prior to running the algorithm. In our case, we choose six clusters, which equates to the number of distinct components in SK394A, including mixed pixels and vesicles (**Fig. 1b**). In the supervised approach, we define the centre based on the mean average of all points belonging to each distinct component in **Figure 1b**. We run both versions of the algorithm for the six elements used in the finite mixture model (**Table 2; Fig. 10**), although the results are similar when using all 10 measured elements (**Supplementary Fig. 8**).

The impact of the porphyritic nature of the samples can be seen in both k-means approaches (**Fig. 10a-b**), in which amphibole has not been distinguished from orthopyroxene, even in the supervised approach. This is because these two phases are more similar in composition than variability within the mixed pixels, especially given that the matrix contains clinopyroxene, which is not present as a phenocryst. Consequently, discrete components identified within mixed pixels and amphibole-orthopyroxene becomes a single cluster. A similar effect can also be seen for oxides and vesicles, although this is resolved using the supervised algorithm. By simply attributing each pixel to the closest centroid, and not running the k-means algorithm we can see that the results are more

similar to those in **Figure 1b**, with both amphibole-orthopyroxene and oxides-vesicles correctly separated (**Fig. 10c**). However, these centroids have been learnt a-priori using our finite mixture model, and would not be available if only relying on a k-means/centroid-based approach.

To the centre right of each image in **Figure 10** is the crystal in **Figures 3-6**, which has not been as efficiently classified compared to our approach. Large mineral inclusions are removed but cracks less than 20μm remain (**Fig. 10a-b**). Using the centroid approach, these mixed features are better resolved (**Fig. 10c**). However, the similarity between the mixed-matrix composition (in which plagioclase dominates), and the rims of many plagioclase phenocrysts, means that plagioclase phenocrysts have only been partially classified. Hence, even if a centroid-based approach is able to classify each of the mineral phases, it will not correctly remove all mixed pixels at the resolution of individual phenocryst. This will influence the efficacy of further analyses, such as the segmentation we have proposed in this manuscript.

4. Conclusions

We have developed a method to optimally segment zoned phenocrysts, based on their chemical composition, at a thin-section scale. This provides a robust approach to distinguish and correlate mineral zonation. We emphasise that the method is semi-autonomous: it requires an understanding of the mineral phases present and the chemical variability characterising them. The methodology is adaptable to different chemical elements and different spatial scales. In this manuscript there has been a focus on chemical maps, but the approach could be calibrated for use with the results of imaging techniques such a cathodoluminescence or backscatter electron.

Our approach is based on a 3-step procedure: (i) classification of mineral phases; (ii) segmentation of intra-crystal zonation; and (iii) correlation of inter-crystal zonation. Independently, the first classification step also provides a method for the separation of mineral phases. Mineral classification using a finite mixture model has wide application in different fields of geology and geoscience. It provides an effective way to remove noisy data associated with mixed pixels, improving efficacy of down-stream analyses. Segmentation of intra-crystal zonation will enable quantification of crystal fracturing and other physical parameters describing mineral textures (Higgins et al., 2021). Segmentation and correlation of zoned crystals has wide application in a variety of mineral sciences, beyond igneous geochemistry and petrology. It allows fingerprinting of

individual crystals (e.g., Higgins et al., 2021) and we believe it will enable automatic sequencing of temporal zonation within crystals.

Acknowledgements:
TS and OH received funding from the European Research Council (ERC) under the European Union's Horizon 2020 research and innovation program (Grant agreement 677493-FEVER – Prof. Luca Caricchi).

Figure captions:

1. (a) Sample location on the island of St. Kitts; (b+c) Phase maps for samples SK394A and SK394C, classified using the finite mixture model approach developed in this manuscript. All white space is classified as vesicles.
2. Finite mixture model using the transformed parameters in Eq. 1-2 for (a-c) Al-Ca and (d-f) Si-Ca in SK394A. (a,d) The classification of the discrete components (colour) in Fig. 1b, plotted in the transformed parameter space and labelled (shape) according to the results of the finite mixture model. (b,e) The different clusters (colour) identified by the finite mixture model; (c,f) The resulting cluster map according the results of the finite mixture model using the identical colour scheme as panels b and c.
3. Example phenocryst in SK394A: (a) Raw counts of Ca measured using the EMPA, with the outline of the crystal in white according to the results of the finite mixture model; (b) the two masks used to run the segmentation algorithm; (c) normalised counts of Ca in Mask 2.
4. Superpixel centroids (a) at initial position and (b) moved to the lowest gradient position in a 3x3 grid. Pixels may move from their original position because (i) they were located in mask 1, but adjacent to a pixel in mask 2, to which it moves to; (ii) on the edge of the phenocryst and so moves to an interior position; or (iii) moves to a low-gradient position within the crystal.
5. Superpixels and their respective centroids after 10 iterations of the segmentation algorithm. Each of the 80 superpixels is a slightly different colour according to the scale. (a) Locations of superpixel centroids for all 10 iterations. Centroids with lower opacity represent previous locations from where the algorithm has converged. Centroids with a red outline represent a final centroid location. (b) Each superpixel outlined in grey, and it's associated centroid. The white box represents the area covered in panel c. (c) The red boxed outline represents a single superpixel (number 16) that is spatially distributed. This will often occur with areas that belong to mask 1, which can be found within and exterior to the crystal.
6. Phenocryst segmented into two zones based of the results of the affinity propagation algorithm. The superpixels are outlined in grey, and two exemplar pixels from the affinity propagation are outlined in red.
7. Correlation of segmented zones, based on (a) the anorthite distribution. The number of zoning groups is chosen manually based on the results of a hierarchical clustering algorithm, and is informed: by (b) quantitative scoring metrics such as the C-Index; and (c) by visually using a distance matrix. The colours to the right of the distance matrix correspond to zoning groups in Figure 8.
8. Correlation of segmented plagioclase in (a) SK394A and (b) SK394C. Across both samples, six zoning groups have been identified, based on (c) the anorthite composition of each zone. The colour of each of the zoning groups corresponds to that plotted next to the distance matrix in Figure 7.
9. Segmented zones in individual plagioclase, where the colour does not represent the correlation of chemistry. Phenocrysts have been split into a maximum of three zones in both (a) SK394A and (b) SK394C. (c-d) The calibrated anorthite composition of segmented plagioclase in both samples, using Eq. 13.

10. Classification of 6 discrete components in SK394A using the six elements in Table 2. The results are for: (a) an unsupervised k-means; (b) a supervised k-means; and (c) a minimisation of the Euclidean distance to the mean value of each discrete component identified in Figure 1a. The mean values used in panel (c) are used to initiate the supervised approach in panel (b).

Tables:

Table 1: Unique cluster-combinations for the five discrete components in SK394A, using the results from the Al-Ca and Si-Ca discrete mixture models in Figure 3

Component	Index (Al-Ca)	Index (Si-Ca)	Combination
Plagioclase	1	1	1-1
Orthopyroxene	3	3	3-3
Amphibole	1	3	1-3
Oxides	3	2	3-2
Vesicles	2	2	2-2

Table 2: Nine combinations of elements used to discretely cluster sample SK394A

Combination	No. of clusters identified	Cumulative combinations of clusters
Al-Ca	4	4
Al-Fe	3	12
Al-K	4	37
Al-Mg	3	106
Si-Al	4	277
Si-Ca	5	582
Si-Fe	3	747
Si-K	6	1464
Si-Mg	1	1464

Supplementary files:

Supplementary Data (Excel file) – Supplementary tables 1-2

Supplementary Figures (PDF file) – Supplementary figures 1-8

References:

Achanta, R., Shaji, A., Smith, K., Lucchi, A., Fua, P., Süsstrunk, S., 2012. SLIC superpixels compared to state-of-the-art superpixel methods. *IEEE transactions on pattern analysis and machine intelligence*, *34*(11), 2274-2282.

Bachmann, O., Dungan, M. A., 2002. Temperature-induced Al-zoning in hornblendes of the Fish Canyon magma, Colorado. *American Mineralogist*, *87*(8-9), 1062-1076.

Bennett, E. N., Lissenberg, C. J., Cashman, K. V., 2019. The significance of plagioclase textures in mid-ocean ridge basalt (Gakkel Ridge, Arctic Ocean). *Contributions to Mineralogy and Petrology*, *174*(6), 1-22.

Bodenhofer, U., Kothmeier, A., Hochreiter, S., 2011. APCluster: an R package for affinity propagation clustering. *Bioinformatics*, *27*(17), 2463-2464.

Cao, M., Evans, N. J., Reddy, S. M., Fougerouse, D., Hollings, P., Saxey, D. W., McInnes, B.I.A., Cooke, D.R., McDonald, B.J., Qin, K. (2019). Micro-and nano-scale textural and compositional zonation in plagioclase at the Black Mountain porphyry Cu deposit: Implications for magmatic processes. *American Mineralogist: Journal of Earth and Planetary Materials*, *104*(3), 391-402.

Cashman, K., Blundy, J., 2013. Petrological cannibalism: the chemical and textural consequences of incremental magma body growth. *Contributions to Mineralogy and Petrology*, *166*(3), 703-729.

Cheng, L., Costa, F., Carniel, R., 2017. Unraveling the presence of multiple plagioclase populations and identification of representative two-dimensional sections using a statistical and numerical approach. *American Mineralogist*, *102*(9), 1894-1905.

Costa, F., Chakraborty, S., 2004. Decadal time gaps between mafic intrusion and silicic eruption obtained from chemical zoning patterns in olivine. *Earth and Planetary Science Letters*, *227*(3-4), 517-530.

Druitt, T. H., Costa, F., Deloule, E., Dungan, M., Scaillet, B., 2012. Decadal to monthly timescales of magma transfer and reservoir growth at a caldera volcano. *Nature*, *482*(7383), 77-80.

Frey, B. J., Dueck, D., 2007. Clustering by passing messages between data points. *science*, *315*(5814), 972-976.

Ginibre, C., Kronz, A., Wörner, G., 2002. High-resolution quantitative imaging of plagioclase composition using accumulated backscattered electron images: new constraints on oscillatory zoning. *Contributions to Mineralogy and Petrology*, *142*(4), 436-448.

Ginibre, C., Wörner, G., Kronz, A., 2007. Crystal zoning as an archive for magma evolution. *Elements*, *3*(4), 261-266.

Gottlieb, P., Wilkie, G., Sutherland, D., Ho-Tun, E., Suthers, S., Perera, K., Jenkins, B., Spencer, S., Butcher, B., Rayner, J., 2000. Using quantitative electron microscopy for process mineralogy applications. *JOM*, *52*(4), 24-25

Hanchar, J. M., Miller, C. F., 1993. Zircon zonation patterns as revealed by cathodoluminescence and backscattered electron images: implications for interpretation of complex crustal histories. *Chemical geology*, *110*(1-3), 1-13.

Higgins, O., Sheldrake, T., Caricchi, L., 2021. Quantitative chemical mapping of plagioclase as a tool for the interpretation of volcanic stratigraphy: an example from St Kitts, Lesser Antilles. *Earth and Planetary Science Letters* (under review).

Hubert, L., Schultz, J., 1976. Quadratic assignment as a general data analysis strategy. *British journal of mathematical and statistical psychology*, *29*(2), 190-241.

Humphreys, M. C., Blundy, J. D., Sparks, R. S. J., 2006. Magma evolution and open-system processes at Shiveluch Volcano: Insights from phenocryst zoning. *Journal of Petrology*, *47*(12), 2303-2334.

Humphreys, M. C. S., Edmonds, M., Plail, M., Barclay, J., Parkes, D., Christopher, T., 2013. A new method to quantify the real supply of mafic components to a hybrid andesite. Contributions to Mineralogy and Petrology, 165(1), 191-215.

Lanari, P., Vidal, O., De Andrade, V., Dubacq, B., Lewin, E., Grosch, E. G., Schwartz, S., 2014. XMapTools: A MATLAB©-based program for electron microprobe X-ray image processing and geothermobarometry. *Computers & Geosciences*, *62*, 227-240.

Lanari, P., Vho, A., Bovay, T., Airaghi, L., Centrella, S., 2019. Quantitative compositional mapping of mineral phases by electron probe micro-analyser. *Geological Society, London, Special Publications*, *478*(1), 39-63.

Lee, M. R., Martin, R. W., Trager-Cowan, C., Edwards, P. R., 2005. Imaging of cathodoluminescence zoning in calcite by scanning electron microscopy and hyperspectral mapping. *Journal of Sedimentary Research*, *75*(2), 313-322.

Leisch, F., 2004. FlexMix: A general framework for finite mixture models and latent class regression in R. *Journal of Statistical Software*, 11 (8), 1-18.

Maitre, J., Bouchard, K., Bédard, L. P., 2019. Mineral grains recognition using computer vision and machine learning. *Computers & Geosciences*, *130*, 84-93.

Melekhova, E., Blundy, J., Martin, R., Arculus, R., Pichavant, M., 2017. Petrological and experimental evidence for differentiation of water-rich magmas beneath St. Kitts, Lesser Antilles. *Contributions to Mineralogy and Petrology*, *172*(11-12), 98.

Pietranik, A., Koepke, J., Puziewicz, J., 2006. Crystallization and resorption in plutonic plagioclase: implications on the evolution of granodiorite magma (Gęsiniec granodiorite, Strzelin Crystalline Massif, SW Poland). *Lithos*, *86*(3-4), 260-280.

Probst, L. C., Sheldrake, T. E., Gander, M. J., Wallace, G., Simpson, G., Caricchi, L., 2018. A cross correlation method for chemical profiles in minerals, with an application to zircons of the Kilgore Tuff (USA). *Contributions to Mineralogy and Petrology*, *173*(3), 23.

Shcherbakov, V. D., Plechov, P. Y., Izbekov, P. E., Shipman, J. S., 2011. Plagioclase zoning as an indicator of magma processes at Bezymianny Volcano, Kamchatka. *Contributions to Mineralogy and Petrology*, *162*(1), 83-99.

Singer, B. S., Dungan, M. A., Layne, G. D., 1995. Textures and Sr, Ba, Mg, Fe, K, and Ti compositional profiles in volcanic plagioclase: clues to the dynamics of calc-alkaline magma chambers. *American Mineralogist*, *80*(7-8), 776-798.

Sisson, T. W., Grove, T. L., 1993. Experimental investigations of the role of H 2 O in calc-alkaline differentiation and subduction zone magmatism. *Contributions to mineralogy and petrology*, *113*(2), 143-166.

Ubide, T., McKenna, C. A., Chew, D. M., Kamber, B. S., 2015. High-resolution LA-ICP-MS trace element mapping of igneous minerals: In search of magma histories. *Chemical Geology*, *409*, 157-168.

Viccaro, M., Giacomoni, P. P., Ferlito, C., Cristofolini, R., 2010. Dynamics of magma supply at Mt. Etna volcano (Southern Italy) as revealed by textural and compositional features of plagioclase phenocrysts. *Lithos*, *116*(1-2), 77-91.

Wallace, G. S., Bergantz, G. W., 2002. Wavelet-based correlation (WBC) of zoned crystal populations and magma mixing. *Earth and Planetary Science Letters*, *202*(1), 133-145.

92 Watt, G. R., Wright, P., Galloway, S., McLean, C., 1997. Cathodoluminescence and trace element
93 zoning in quartz phenocrysts and xenocrysts. *Geochimica et Cosmochimica Acta*, *61*(20), 4337-4348.

94 Weber, G., Arce, J. L., Ulianov, A., Caricchi, L., 2019. A Recurrent Magmatic Pattern on Observable
95 Timescales Prior to Plinian Eruptions From Nevado de Toluca (Mexico). *Journal of Geophysical*
96 *Research: Solid Earth*, *124*(11), 10999-11021.

97 Willis, K. V., Srogi, L., Lutz, T., Monson, F. C., Pollock, M., 2017. Phase Composition Maps integrate
98 mineral compositions with rock textures from the micro-meter to the thin section scale. *Computers*
99 *& Geosciences*, *109*, 162-177.

00 Wilson, N. C., MacRae, C. M., 2005. An automated hybrid clustering technique applied to spectral
01 data sets. *Microscopy and Microanalysis*, *11*(S02), 434-435.

02 Zellmer, G. F., Sparks, R. S. J., Hawkesworth, C. J., Wiedenbeck, M., 2003. Magma emplacement and
03 remobilization timescales beneath Montserrat: insights from Sr and Ba zonation in plagioclase
04 phenocrysts. *Journal of Petrology*, *44*(8), 1413-1431.

05 Zhou, B., 2015. Image segmentation using SLIC superpixels and affinity propagation clustering. *Int.*
06 *J. Sci. Res*, *4*(4), 1525-1529.

Figure 1

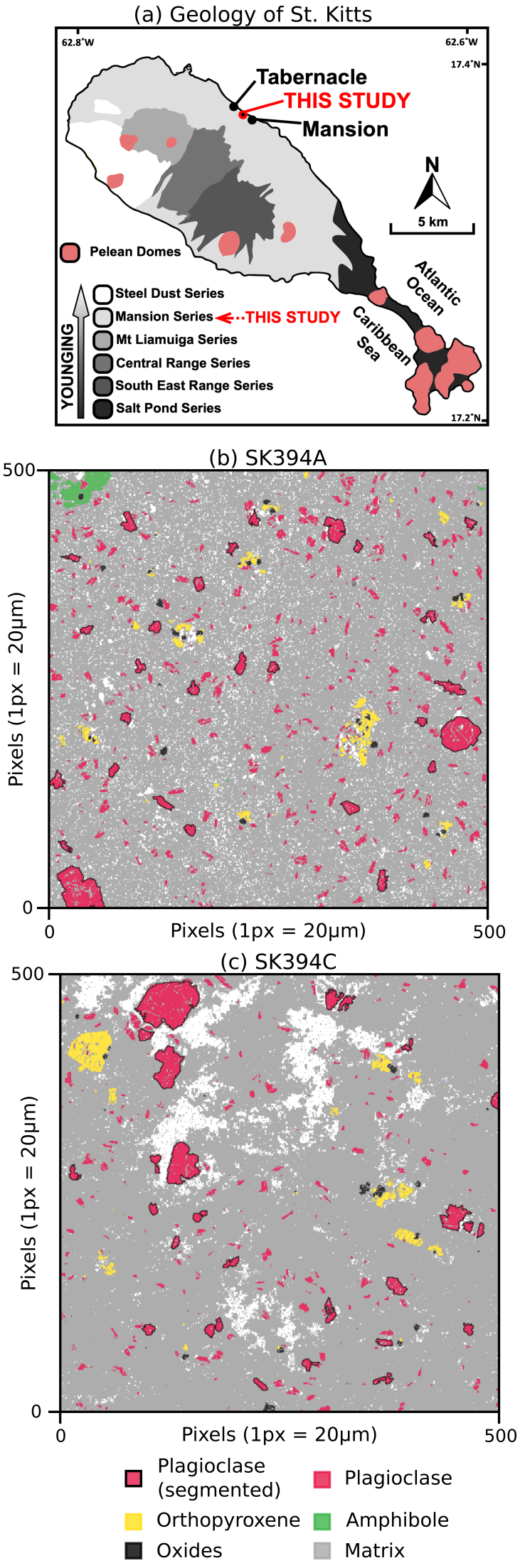
(a) Geology of St. Kitts
62.8°W
62.6°W
17.4°N
17.2°N
Tabernacle
THIS STUDY
Mansion
N
5 km
Pelean Domes
Steel Dust Series
Mansion Series
THIS STUDY
Mt Liamuiga Series
Central Range Series
South East Range Series
Salt Pond Series
YOUNGING
Atlantic Ocean
Caribbean Sea
(b) SK394A
Pixels (1px = 20µm)
0
500
(c) SK394C
Plagioclase (segmented)
Plagioclase
Orthopyroxene
Amphibole
Oxides
Matrix

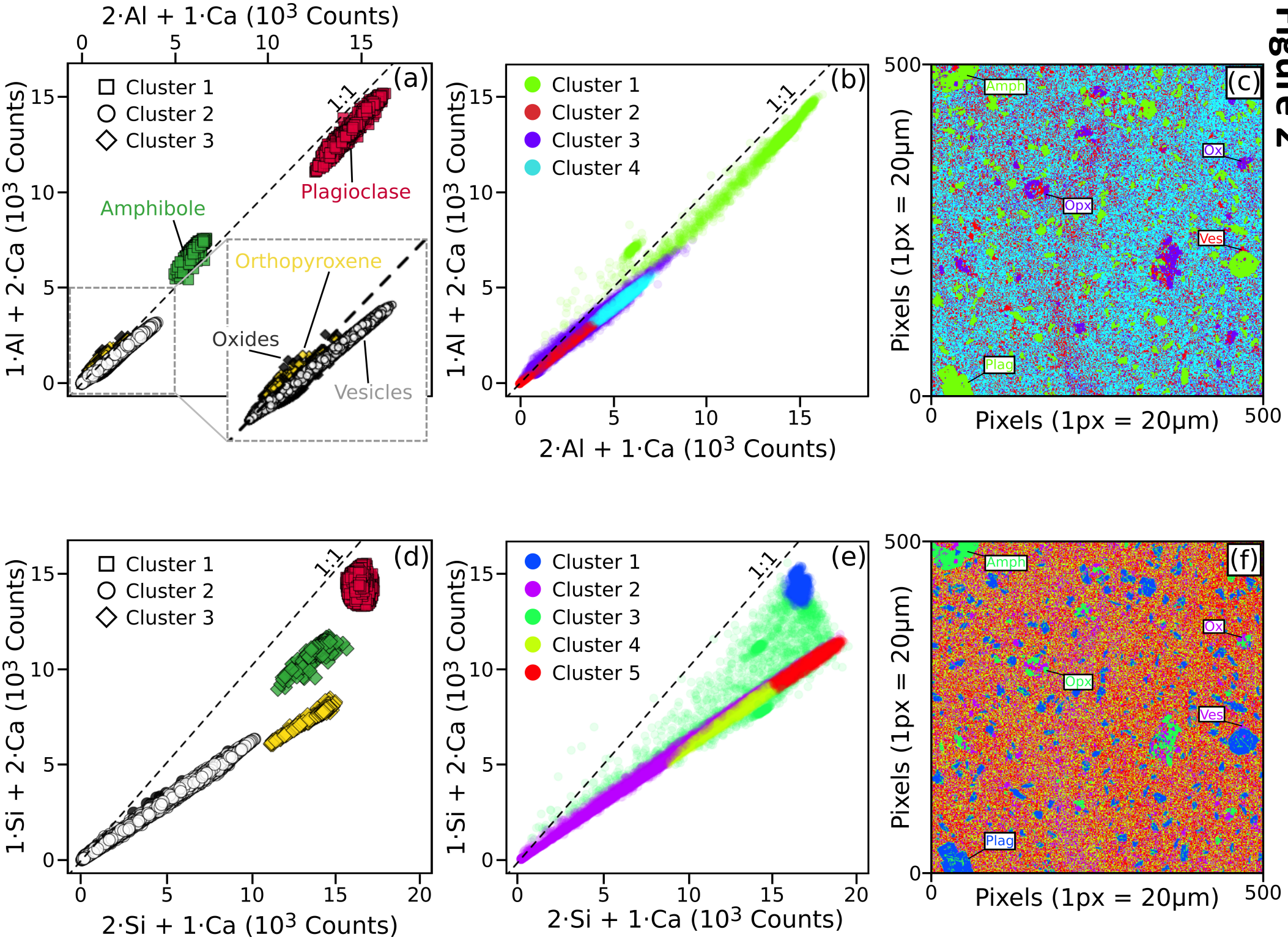
Figure 2
(a)
(b)
(c)
(d)
(e)
(f)
2·Al + 1·Ca (10³ Counts)
1·Al + 2·Ca (10³ Counts)
2·Si + 1·Ca (10³ Counts)
1·Si + 2·Ca (10³ Counts)
Pixels (1px = 20µm)
Cluster 1
Cluster 2
Cluster 3
Cluster 4
Cluster 5
1:1
Plagioclase
Amphibole
Orthopyroxene
Oxides
Vesicles
Amph
Ox
Opx
Ves
Plag

Figure 3

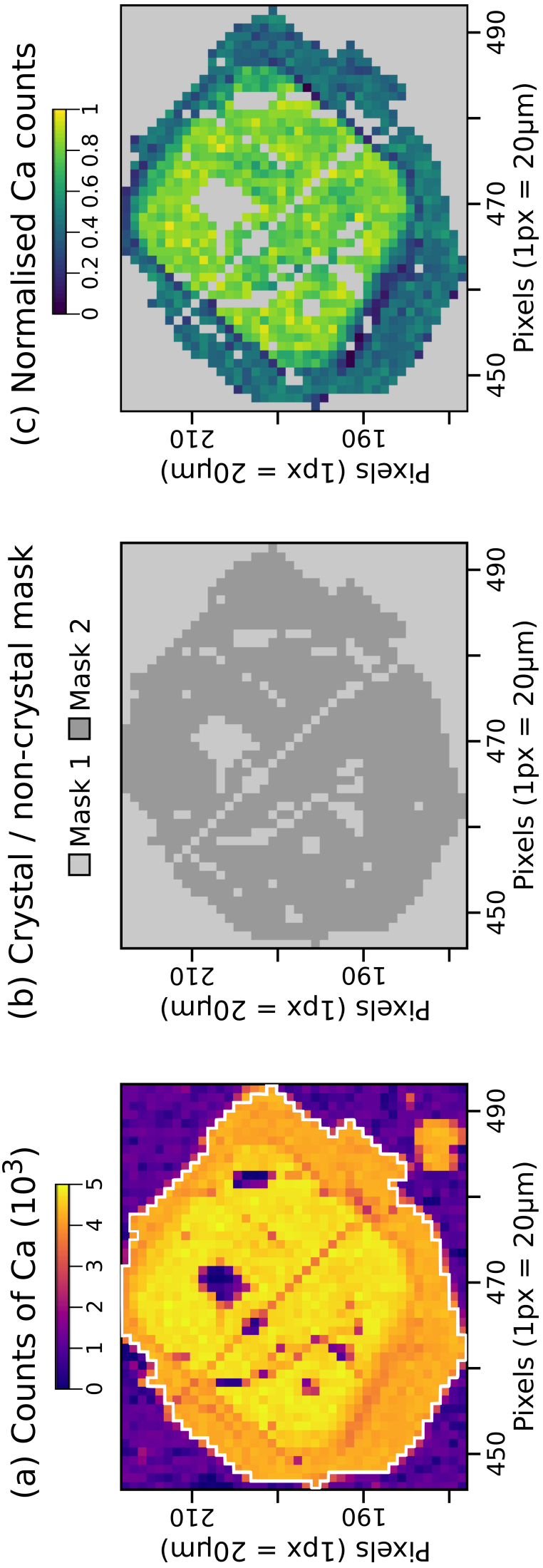
(a) Counts of Ca (10^3)
0
1
2
3
4
5
(b) Crystal / non-crystal mask
Mask 1
Mask 2
(c) Normalised Ca counts
0
0.2
0.4
0.6
0.8
1
Pixels (1px = 20μm)
190
210
450
470
490
Pixels (1px = 20μm)

Figure 4

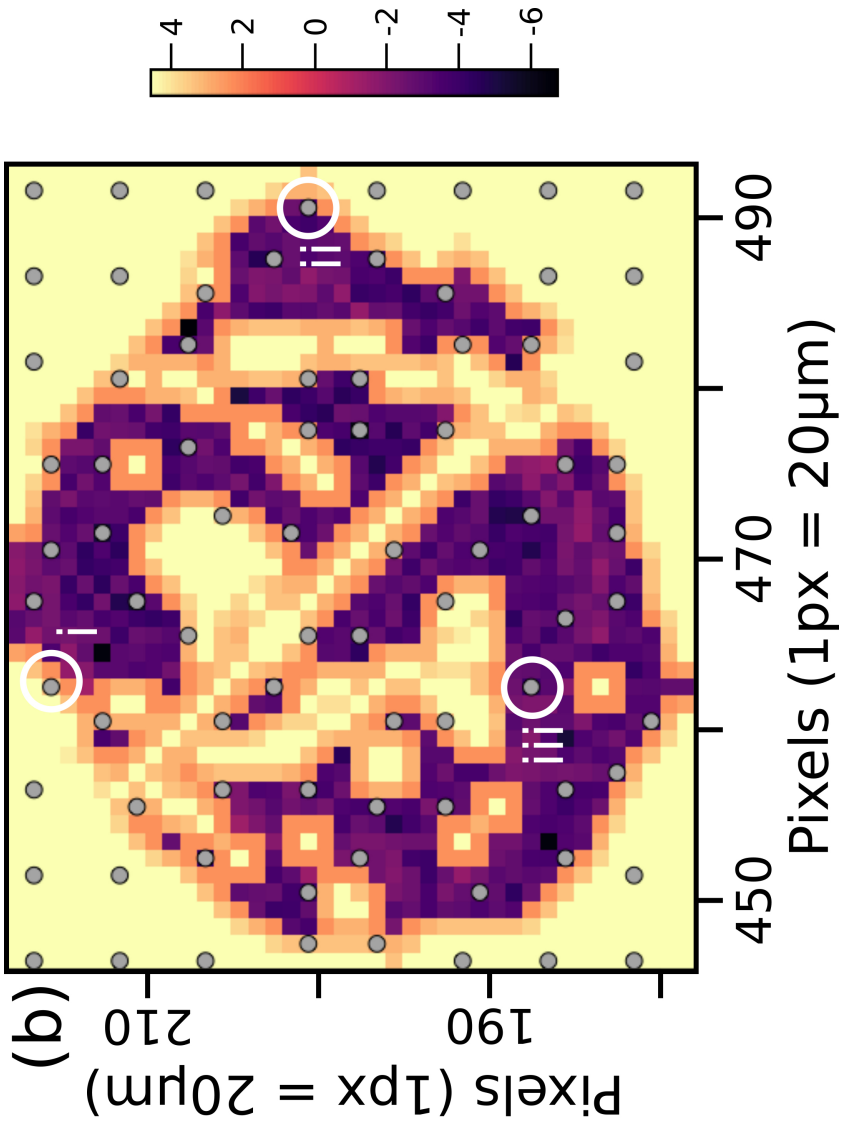
4
2
0
-2
-4
-6
i
ii
iii
(b)
190
210
Pixels (1px = 20μm)
450
470
490
Pixels (1px = 20μm)
(a)
190
210
Pixels (1px = 20μm)
450
470
490
Pixels (1px = 20μm)

Figure 5

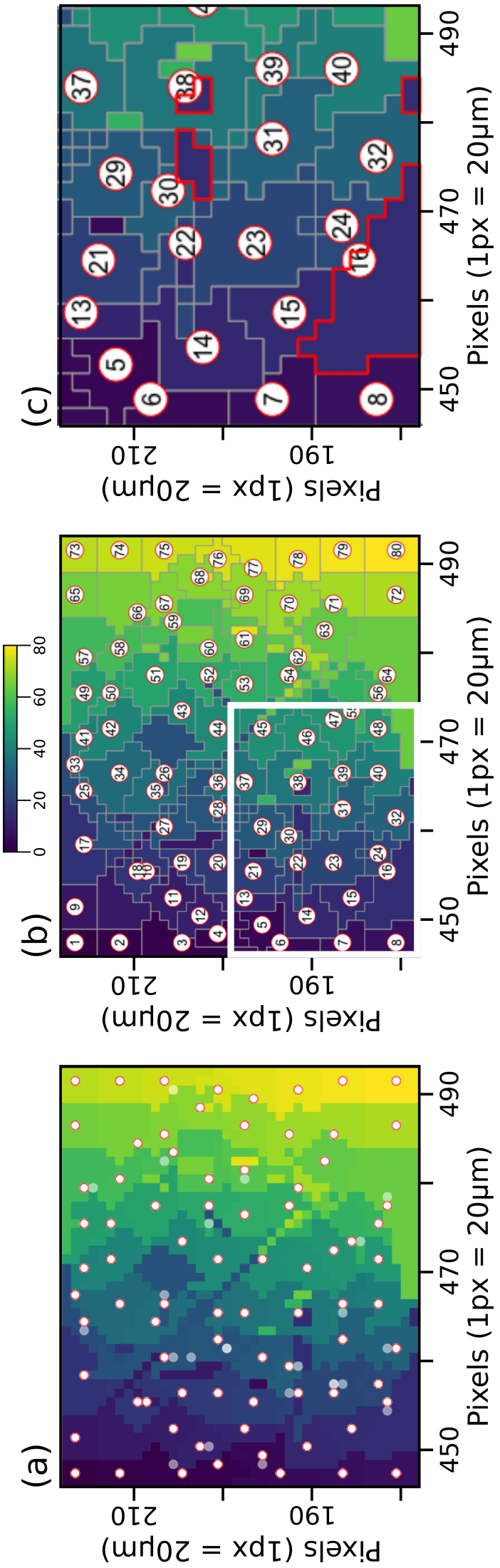

Figure 6

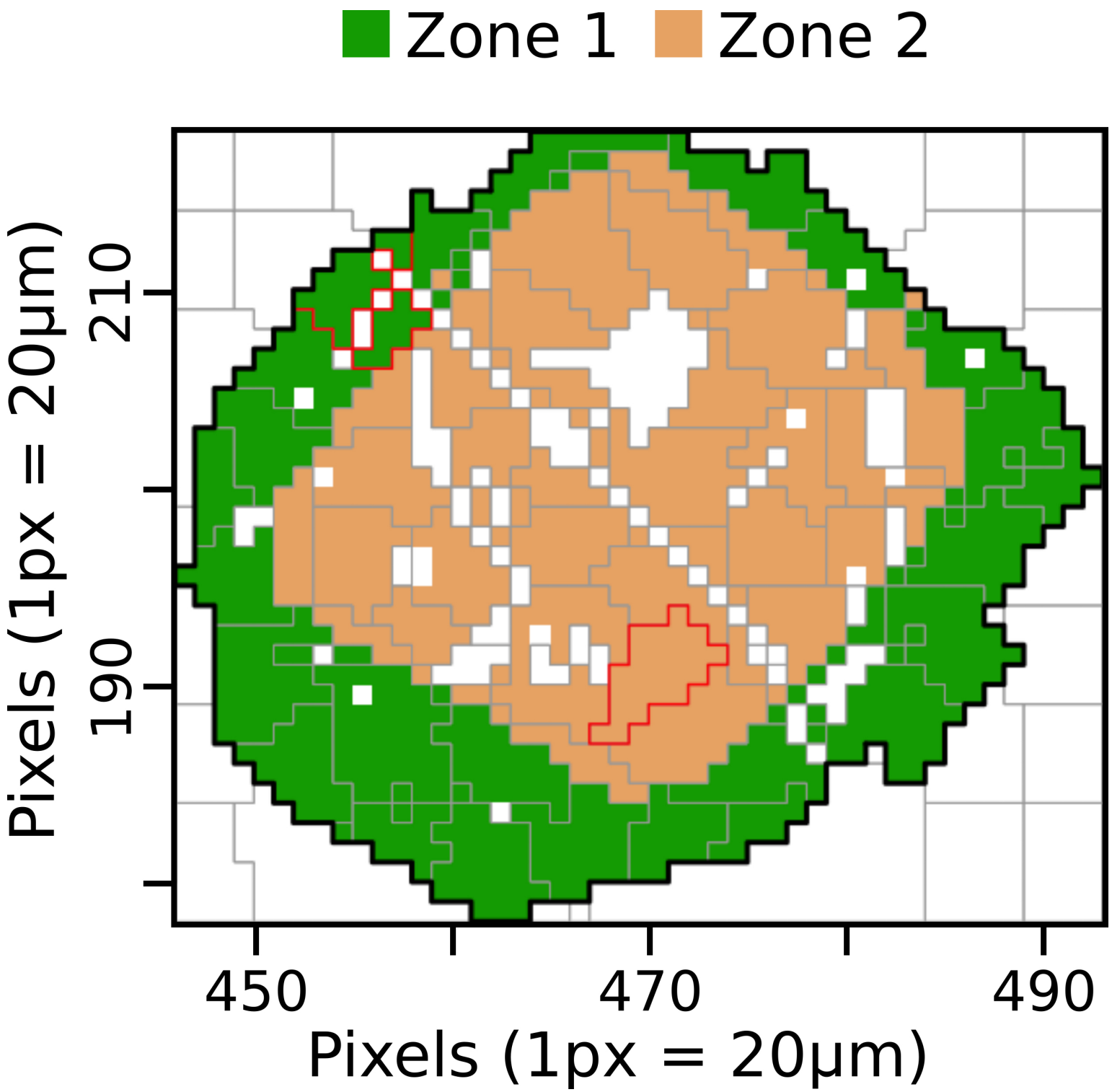
Zone 1
Zone 2
Pixels (1px = 20µm)
210
190
450
470
490
Pixels (1px = 20µm)

Figure 7

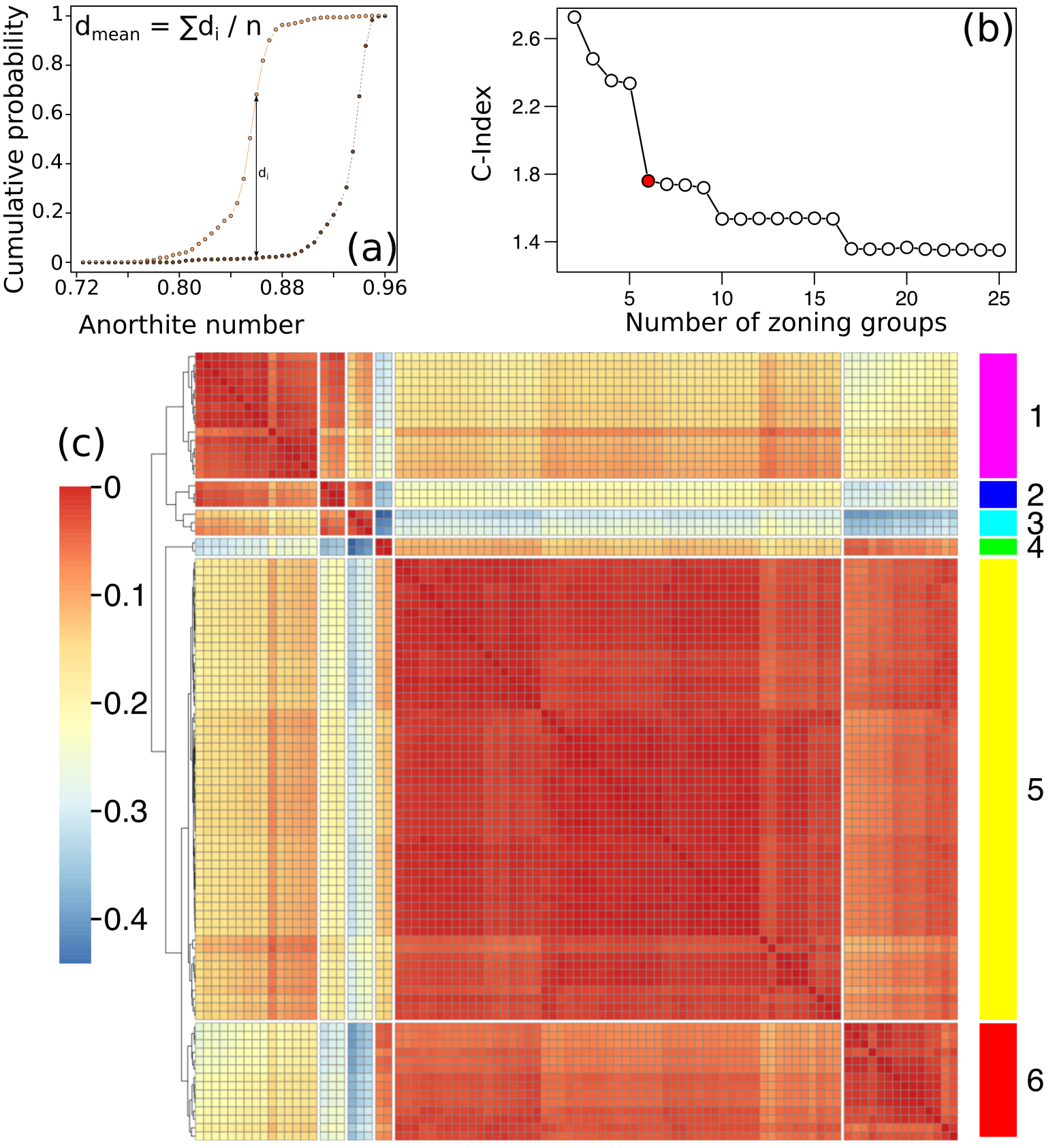
Cumulative probability
1
0.8
0.6
0.4
0.2
0
$d_{mean} = \Sigma d_i / n$
d_i
(a)
0.72
0.80
0.88
0.96
Anorthite number
C-Index
2.6
2.2
1.8
1.4
(b)
5
10
15
20
25
Number of zoning groups
(c)
0
-0.1
-0.2
-0.3
-0.4
1
2
3
4
5
6

Figure 8

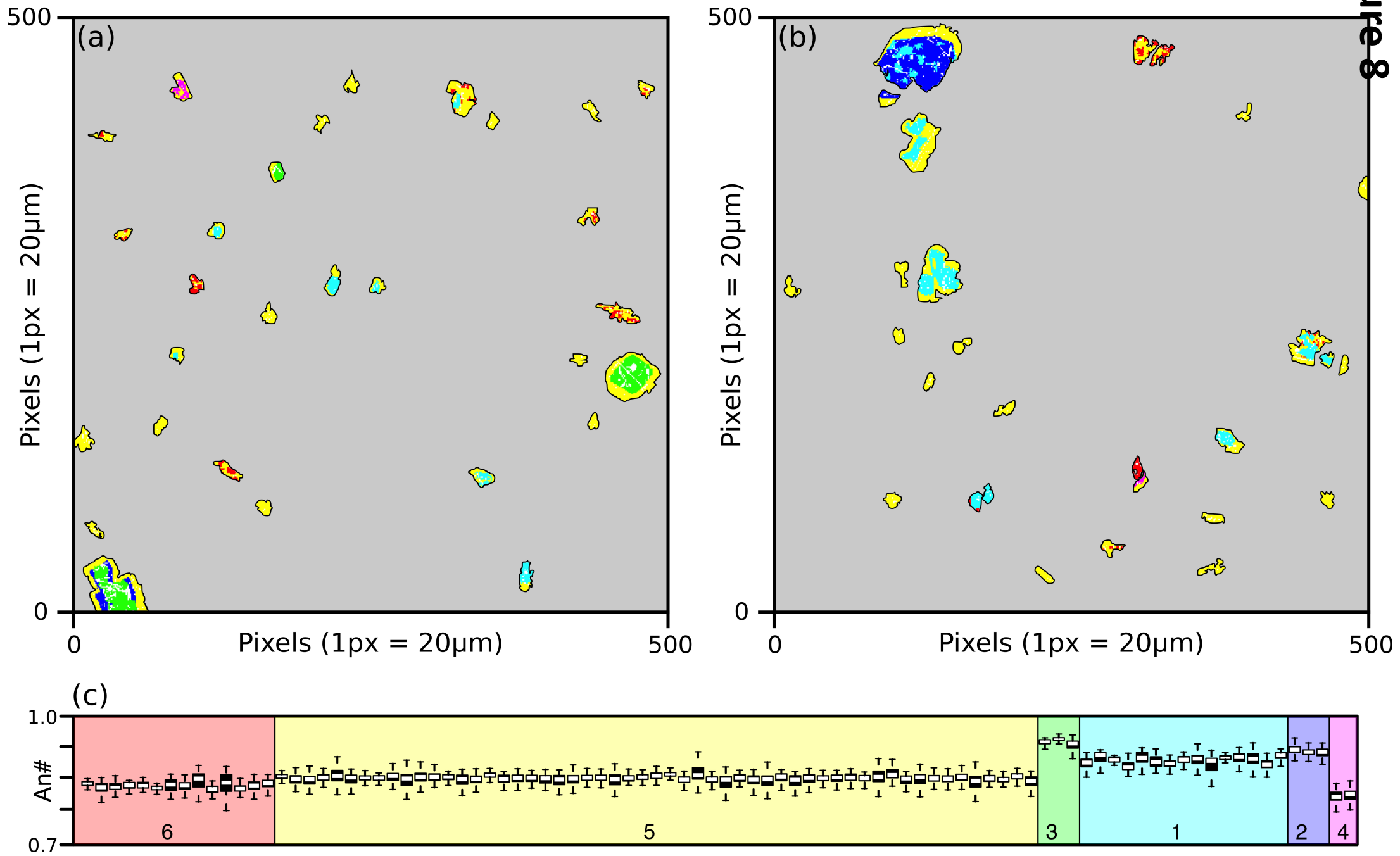

Figure 9

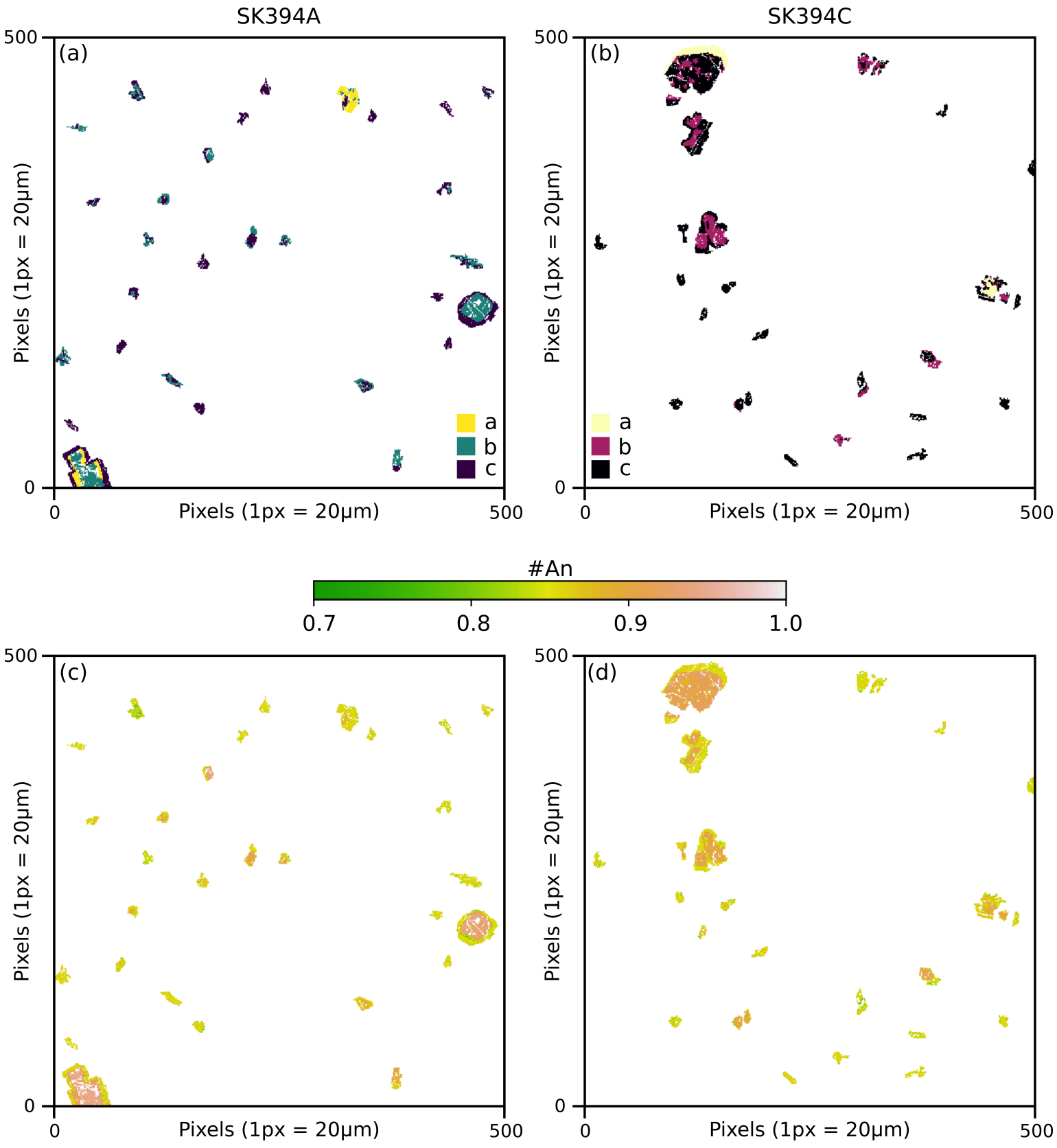

Figure 10

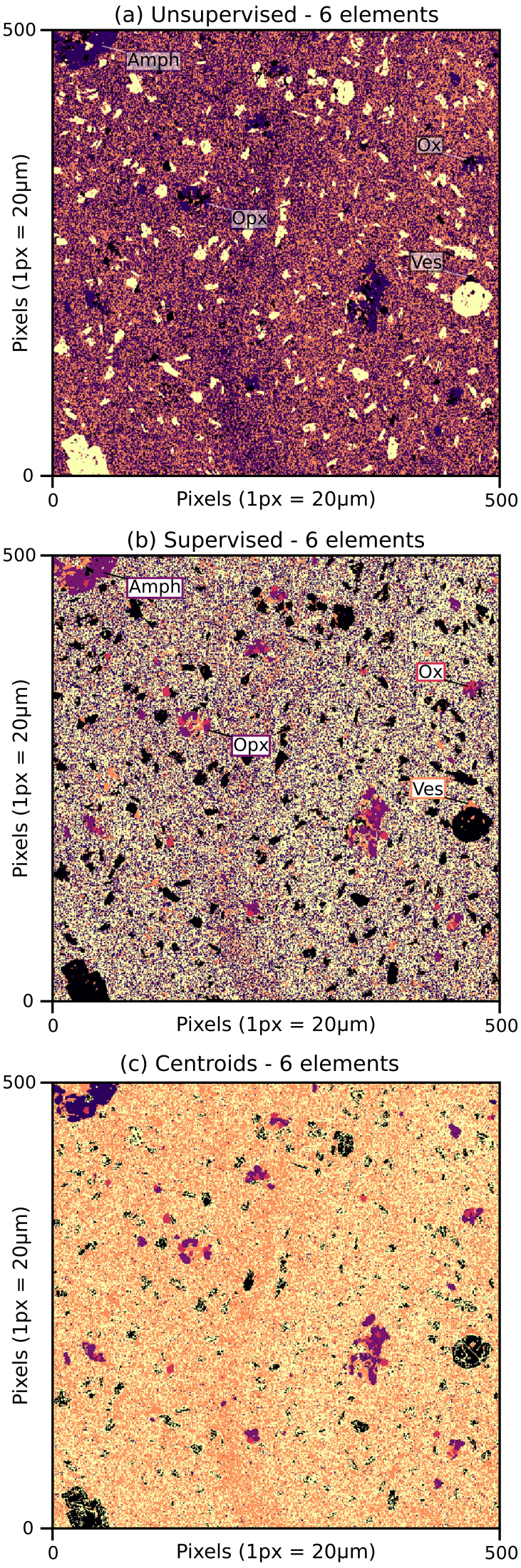
(a) Unsupervised - 6 elements
Amph
Ox
Opx
Ves
500
0
Pixels (1px = 20µm)
0
500
Pixels (1px = 20µm)
(b) Supervised - 6 elements
Amph
Ox
Opx
Ves
500
0
Pixels (1px = 20µm)
0
500
Pixels (1px = 20µm)
(c) Centroids - 6 elements
500
0
Pixels (1px = 20µm)
0
500
Pixels (1px = 20µm)

Supplementary Figures (PDF file)

Supplementary figures 1-8

Fig. S1: Plagioclase systematics. Ternary diagram of the three plagioclase-feldspar endmembers (Albite, Orthoclase & Anorthite). Positive correlation of atoms per formula unit between Al & Ca. Negative correlation of atoms per formula unit between Al & Si.

Fig. S2: Results of the individual finite mixture models for all combinations of elements in Table 2.

Fig. S3: Finite mixture model classification for (a-b) Si-Cr, and (c-d) Al-Cr. Segmented plagioclase are outlined in dark grey. Phases are only identified when there is significant variability in the network forming cation. Cr has no influence on the results of the finite mixture model.**Fig. S4:** The eight final discrete components that satisfy the *central pixel assumption* in SK394A.

Fig. S5: Results of the affinity propagation for different percentile values ($1/2^{th}$, $1/4^{th}$, $1/20^{th}$, $1/100^{th}$). You can see that for high percentile values the AP algorithm can segment the crystals into many zones, even over-fitting large crystals (e.g., i & ii). Higher percentile values can provide more information on crystal structure (e.g., iii – here the low Ca region in Figure 3 is identified), but may still over-segment noisy crystals (e.g., iv). Choosing too low values will reduce the number of potential zones, especially in larger crystals (e.g., v).

Fig. S6: Calibration of Si, Al, Ca, Na & K in plagioclase for the chemical maps. Outliers in red have been identified using the Cooks distance, and are not included in the calibration.

Fig. S7: Correlation of phenocryst zones when the results of the hierarchical clustering are split into five groups.

Fig. S8: Classification of 6 discrete components in SK394A using: (a) unsupervised k-means; (b) supervised k-means; and (c) a minimisation of the Euclidean distance to the mean value of each discrete component identified in Figure 1a. The mean values used in panel (c) are used to initiate the supervised approach in panel (b). All ten measured oxides have been used.

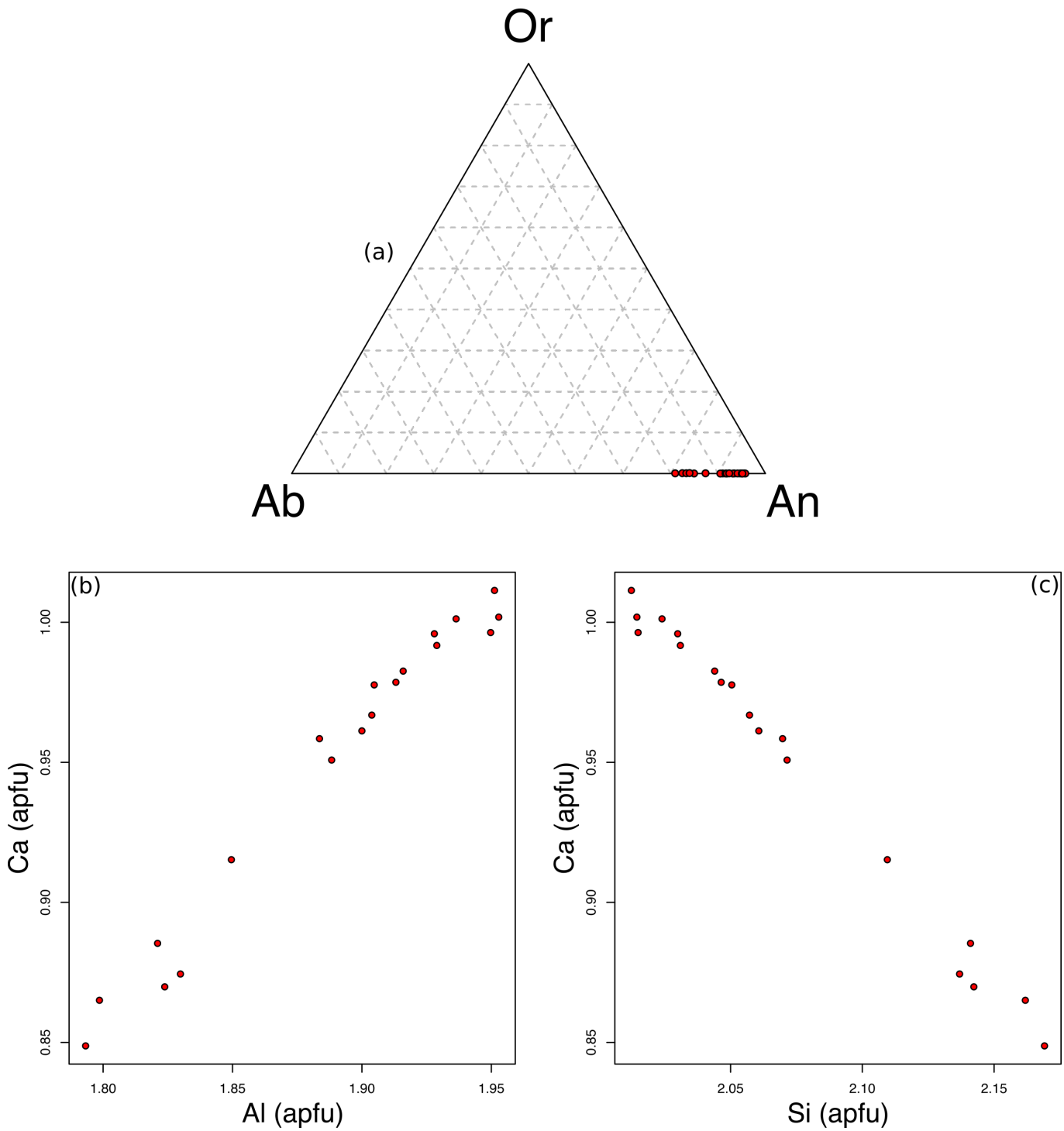

Fig. S1: Plagioclase systematics: (a) Ternary diagram of the three plagioclase-feldspar endmembers (Albite, Orthoclase & Anorthite); (b) Positive correlation of atoms per formula unit between Al & Ca; (c) Negative correlation of atoms per formula unit between Al & Si.

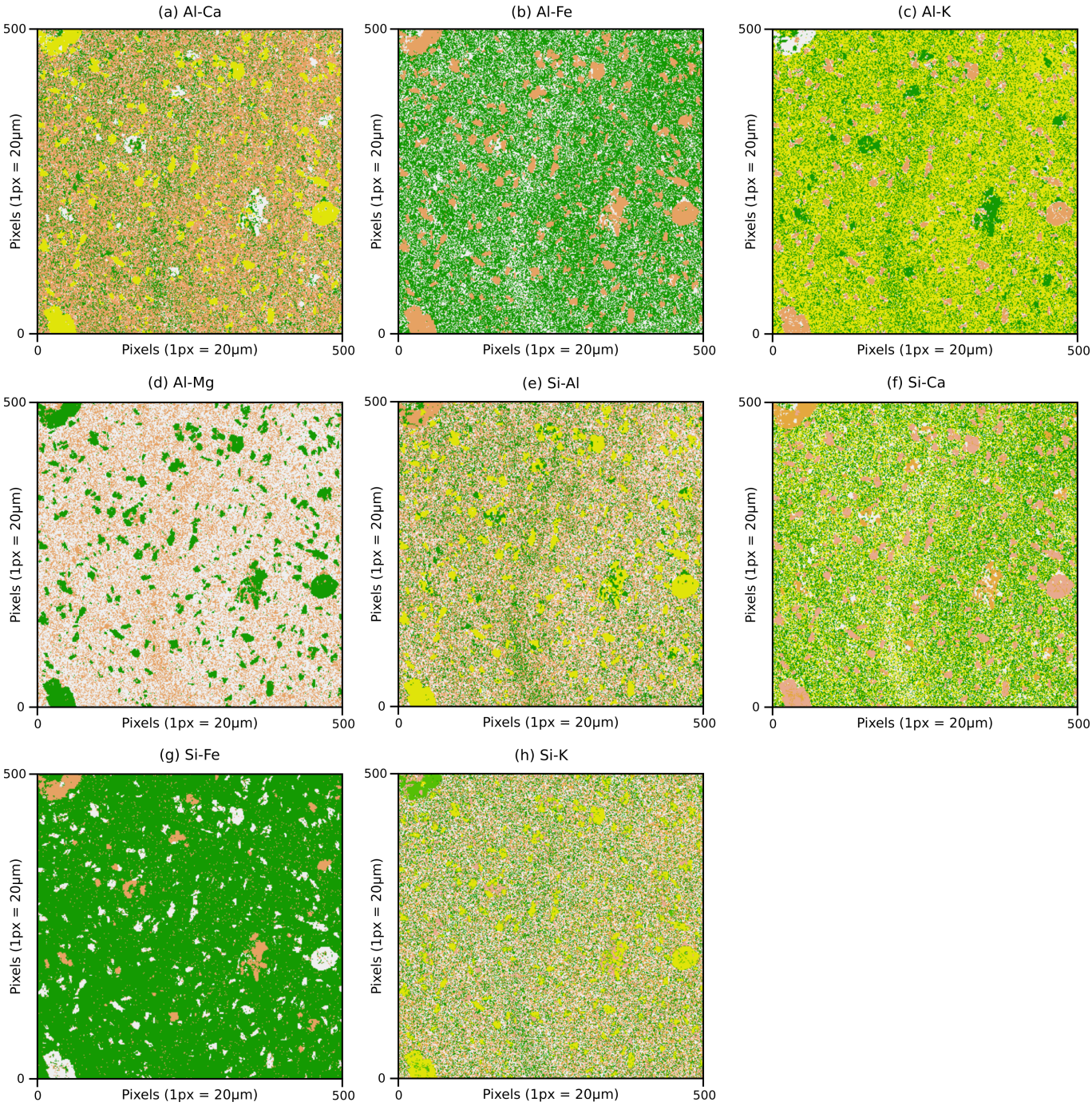

Fig. S2: Results of the individual finite mixture models for all combinations of elements in Table 2.

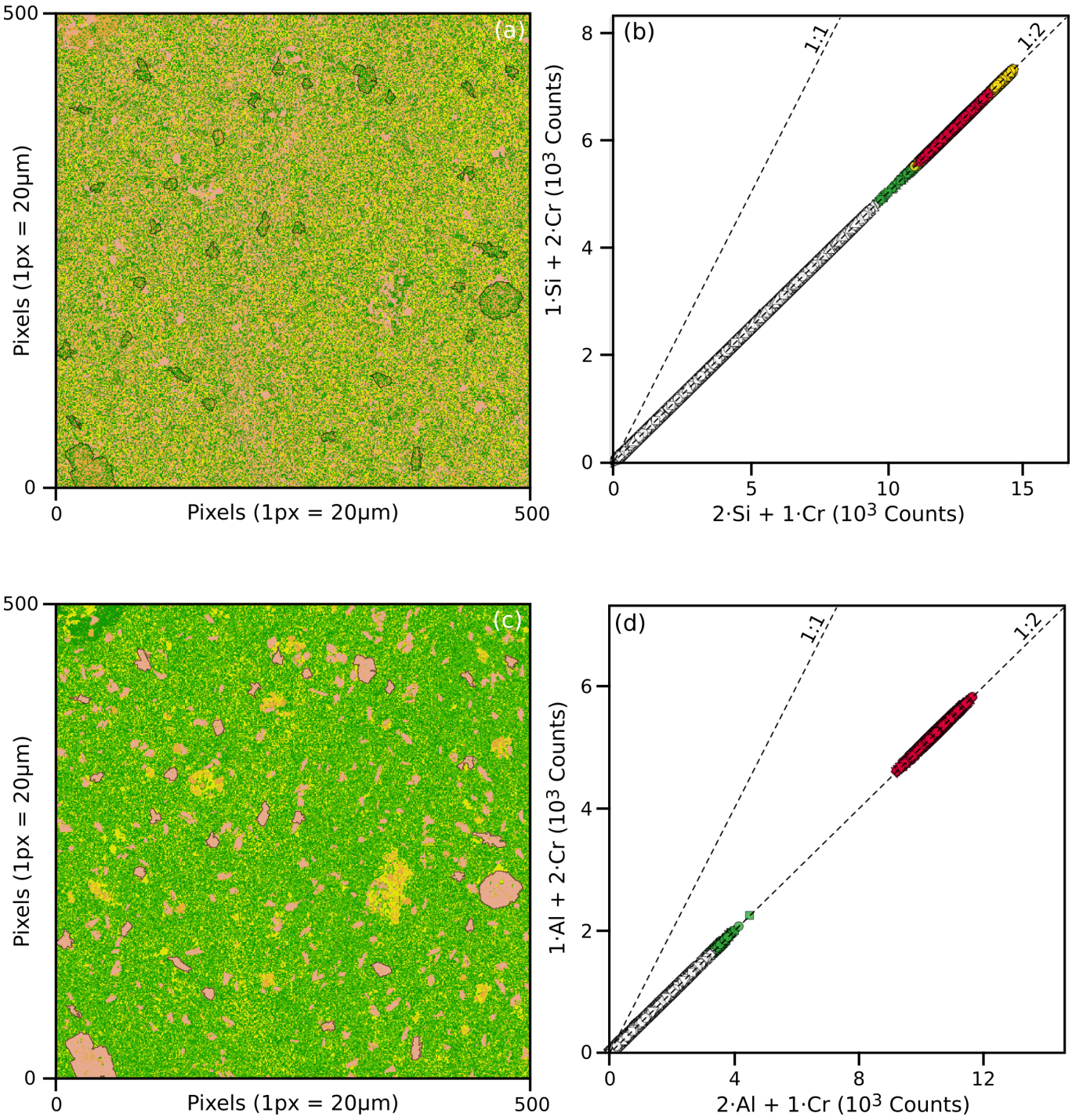

Fig. S3: Finite mixture model classification for (a-b) Si-Cr, and (c-d) Al-Cr. Segmented plagioclase are outlined in dark grey. Phases are only identified when there is significant variability in the network forming cation. Cr has no influence on the results of the finite mixture model.

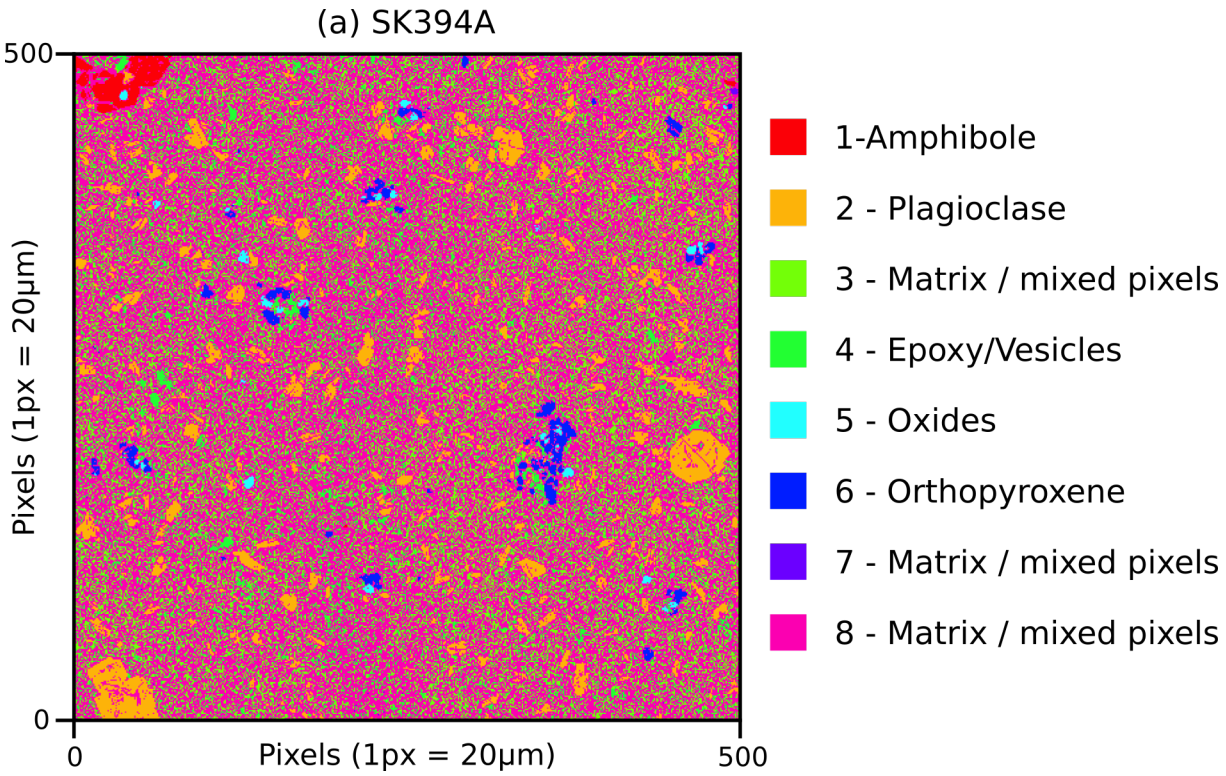

Fig. S4: The eight final discrete components that satisfy the *central pixel assumption* in SK394A.

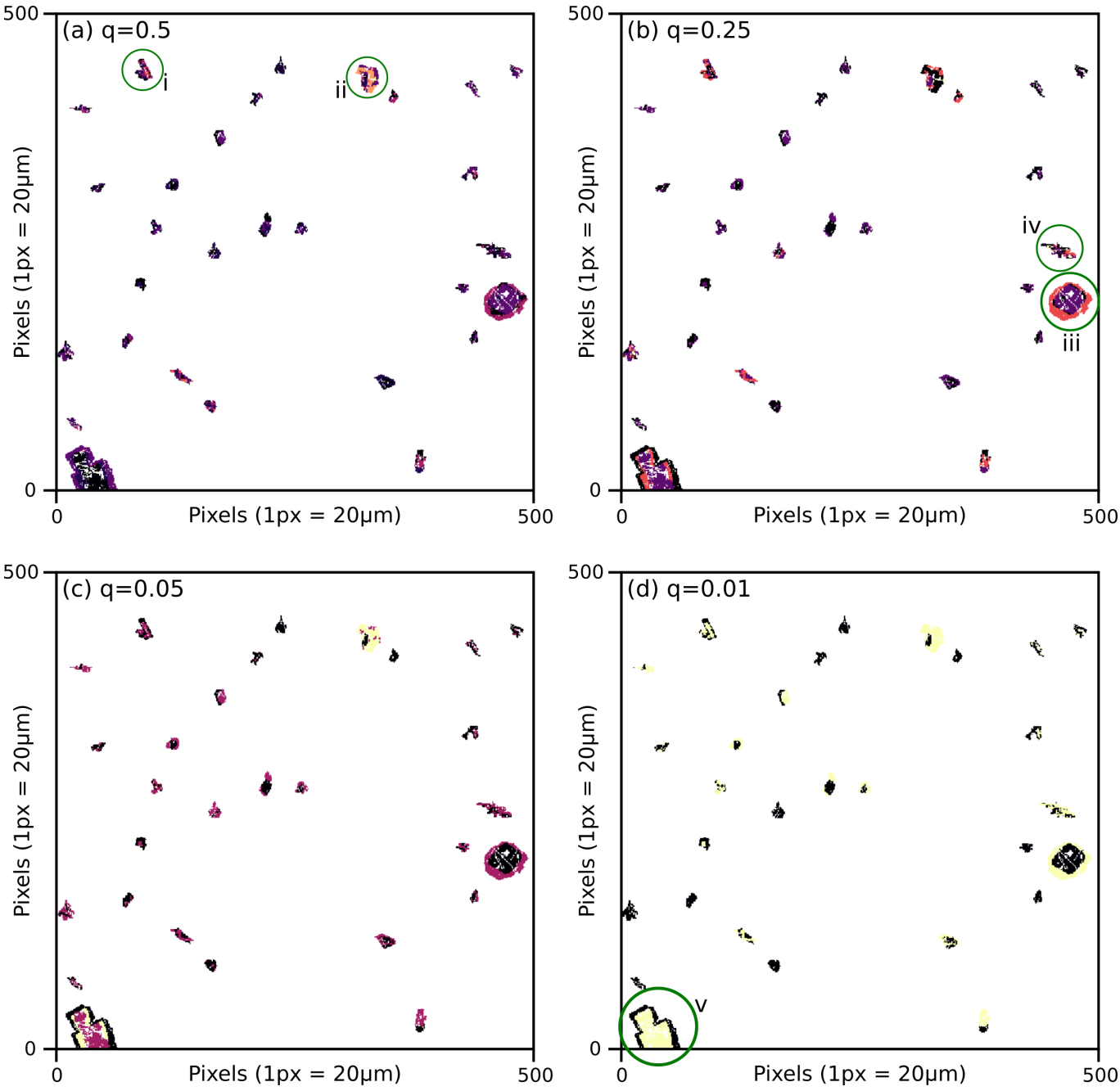

Fig. S5: Results of the affinity propagation for different percentile values (1/2th, 1/4th, 1/20th, 1/100th). You can see that for high percentile values the AP algorithm can segment the crystals into many zones, even over-fitting large crystals (e.g., i & ii). Higher percentile values can provide more information on crystal structure (e.g., iii – here the low Ca region in Figure 3 is identified), but may still over-segment noisy crystals (e.g., iv). Choosing too low values will reduce the number of potential zones, especially in larger crystals (e.g., v).

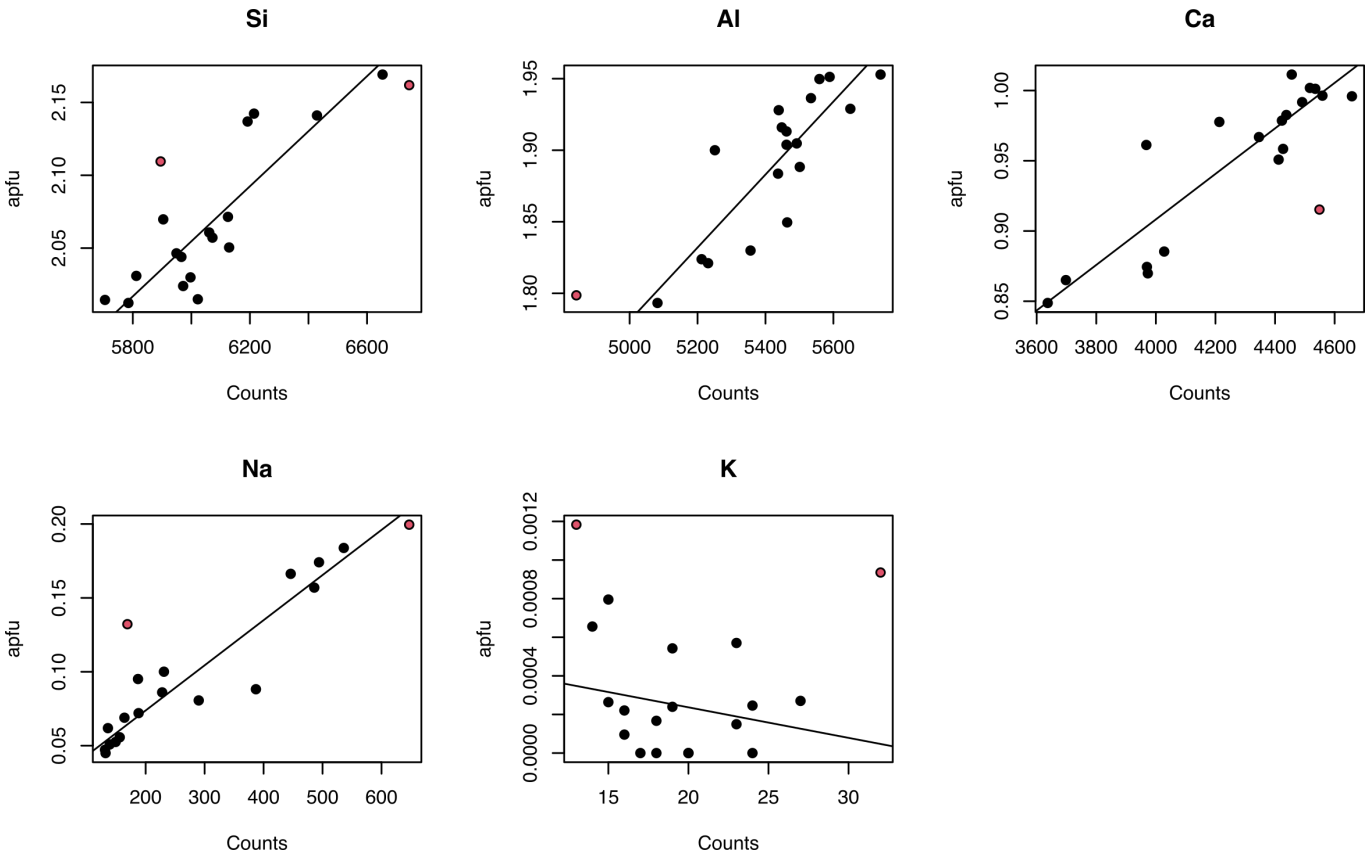

Fig. S6: Calibration of Si, Al, Ca, Na & K in plagioclase for the chemical maps. Outliers in red have been identified using the Cooks distance, and are not included in the calibration.

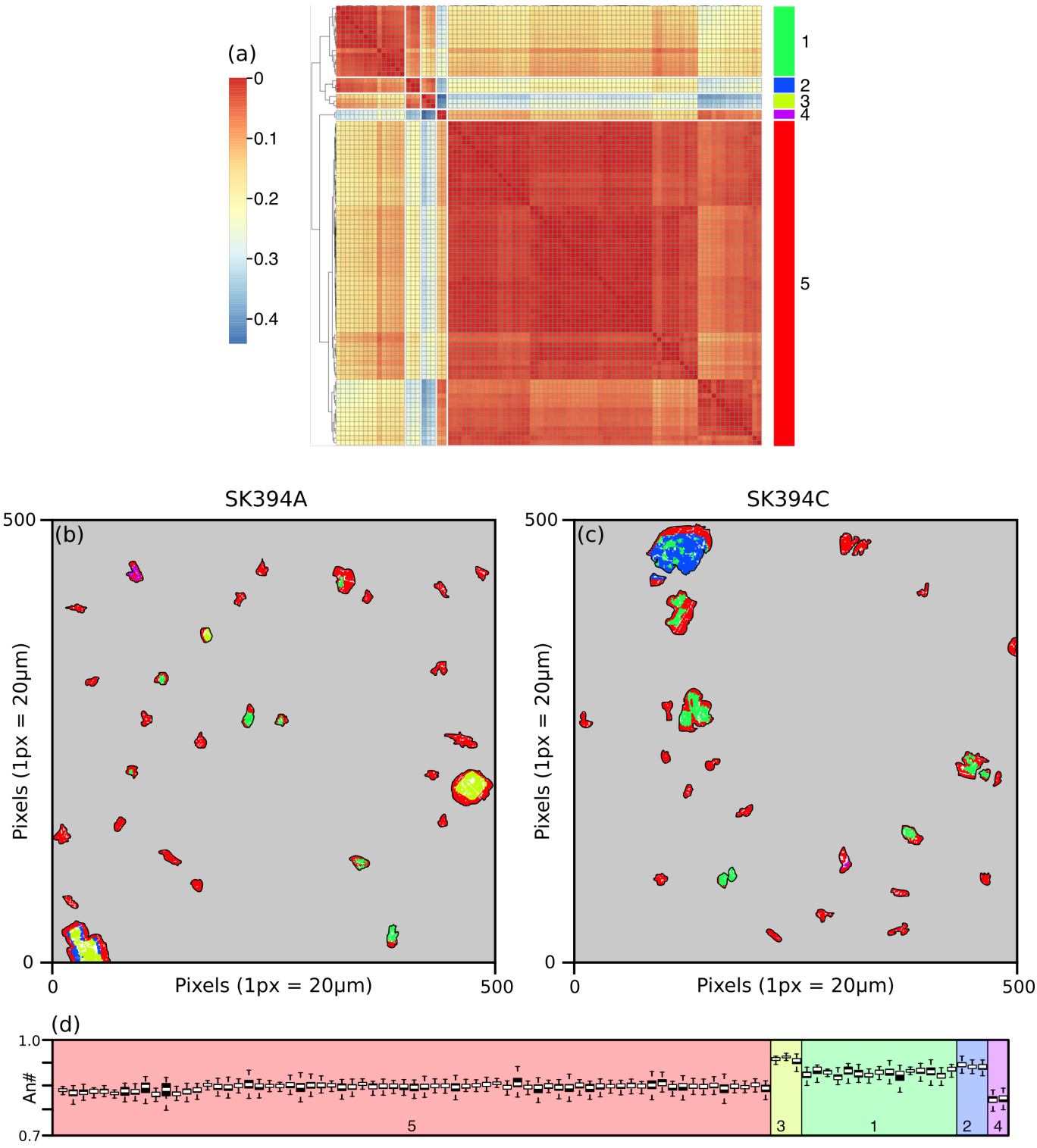

Fig. S7: Correlation of phenocryst zones when the results of the hierarchical clustering are split into five groups.

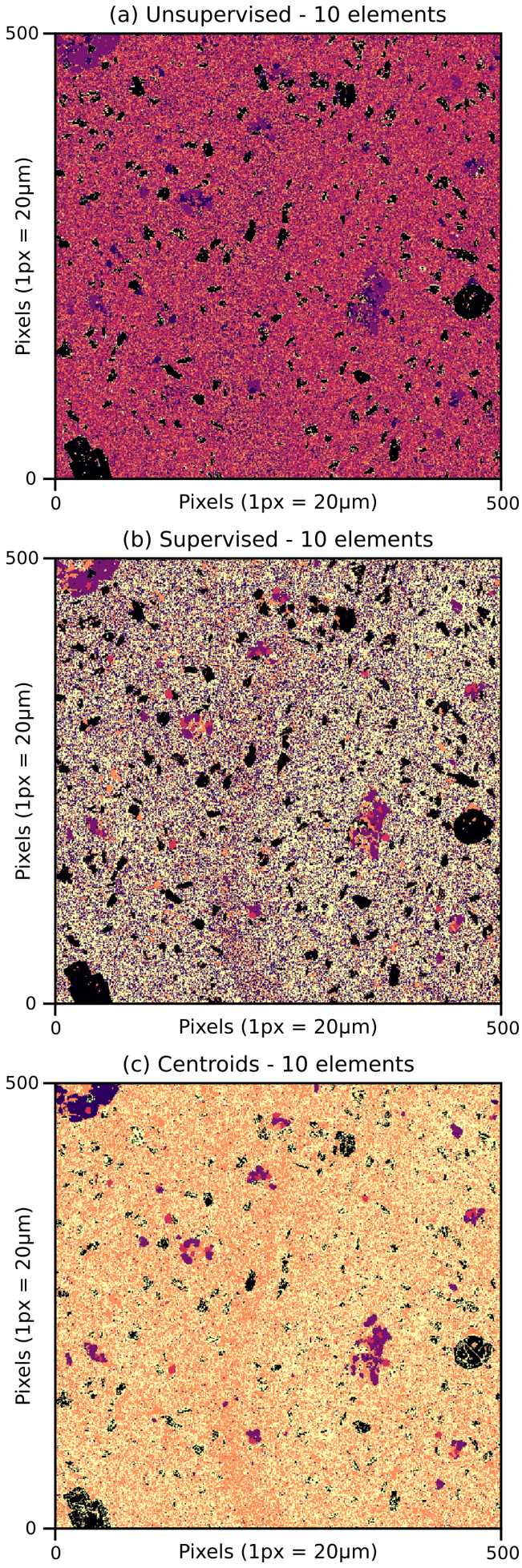

Fig. S8: Classification of 6 discrete components in SK394A using: (a) unsupervised k-means; (b) supervised k-means; and (c) a minimisation of the Euclidean distance to the mean value of each discrete component identified in Figure 1a. The mean values used in panel (c) are used to initiate the supervised approach in panel (b). All ten measured oxides have been used.

Table S1: 1. Results of the finite mixture models for SK394A & SK394C,
including whether the finite mixture model converged and if the results were included in the final classification of the thin section.

SK394A

	1	**2**	**3**	**4**	**5**	**6**	**7**	**8**	**9**
Elements1	Al	Al	Al	Al	Al	Si	Si	Si	Si
Elements2	Ca	Fe	K	Mg	Si	Ca	Fe	K	Mg
Converged	TRUE	TRUE	TRUE	TRUE	TRUE	TRUE	TRUE	TRUE	TRUE
Included	TRUE	TRUE	TRUE	TRUE	TRUE	TRUE	TRUE	TRUE	TRUE
Clusters	4	3	4	3	4	5	3	6	1

SK394C

	1	**2**	**3**	**4**	**5**	**6**	**7**	**8**	**9**
Elements1	Al	Al	Al	Al	Al	Si	Si	Si	Si
Elements2	Ca	Fe	K	Mg	Si	Ca	Fe	K	Mg
Converged	TRUE	TRUE	TRUE	TRUE	FALSE	TRUE	TRUE	TRUE	TRUE
Included	TRUE	TRUE	TRUE	TRUE	FALSE	TRUE	TRUE	TRUE	TRUE
max.Nk	4	3	4	4	5	5	2	4	2

Table S2: Composition of plagioclase point analyses in SK394A

Spot analyses - Oxides (wt. %)									
SiO2	Al2O3	Na2O	MgO	K2O	MnO	CaO	TiO2	FeO	Cr2O3
43.42	34.53	0.755	0.02	0.0045	0.0194	19.48	0.0186	0.4444	0
43.2	34.81	0.611	0.0426	0.0044	0	19.78	0.0058	0.5318	0
44.01	33.98	1.0429	0.0528	0.0041	0.0207	19.02	0.0297	0.5688	0
44.26	34.23	1.1026	0.0326	0	0.0079	18.96	0.024	0.4815	0.0119
46.3	32.68	2.03	0.0386	0.0157	0.014	17.29	0.0119	0.433	0
46.05	33.26	1.93	0.0331	0.0134	0	17.45	0	0.4745	0.0286
45.76	33.02	1.73	0.0223	0.0028	0.0152	17.66	0.0099	0.4959	0.0022
43.99	34.41	0.971	0.0287	0.0025	0.0049	19.15	0.0074	0.5221	0
43.09	35.44	0.5207	0.009	0.0037	0.0194	20	0	0.3545	0.018
42.96	35.34	0.4953	0.0144	0.0016	0.0237	20.15	0.0064	0.31	0
43.75	34.35	0.9439	0.0249	0	0.0177	19.19	0	0.4465	0
46.58	32.67	2.21	0.0382	0.0096	0.0042	17.01	0.0228	0.4778	0
45.85	33.31	1.84	0.0284	0.0199	0.0104	17.51	0.0225	0.4931	0
45.17	33.6	1.46	0.0367	0.011	0.0049	18.29	0.0129	0.5466	0
43.65	34.62	0.7922	0.0203	0	0	19.48	0.0056	0.5365	0
43.25	34.85	0.6795	0.0219	0.004	0.0042	19.71	0	0.5152	0
43.17	35.04	0.5776	0.0344	0	0.0092	19.93	0.0025	0.4158	0.013
43.23	35.49	0.5624	0.0277	0	0.0319	19.95	0.0028	0.5251	0
43.89	34.59	0.89	0.0218	0.0091	0.0362	19.53	0.0183	0.4986	0

Elemental maps (WDS) - Counts (Total)						Spot analyses - Ator				
Si	Al	Ca	Na	K		Si	Al	Na	Mg	K
5966	5448	4438	164	27		2.04396	1.91594	0.06891	0.00140	0.00027
5997	5439	4658	156	15		2.02993	1.92798	0.05567	0.00298	0.00026
5904	5437	4427	187	24		2.06974	1.88360	0.09510	0.00370	0.00025
6125	5501	4412	231	17		2.07145	1.88831	0.10006	0.00227	0.00000
6744	4843	3698	536	32		2.16186	1.79859	0.18379	0.00269	0.00094
6214	5212	3973	494	15		2.14232	1.82381	0.17410	0.00229	0.00080
6429	5231	4028	486	18		2.14106	1.82105	0.15695	0.00155	0.00017
6061	5251	3968	387	23		2.06072	1.89999	0.08820	0.00200	0.00015
5705	5739	4517	131	16		2.01444	1.95287	0.04720	0.00063	0.00022
5785	5589	4456	132	16		2.01235	1.95123	0.04499	0.00101	0.00010
6072	5462	4346	228	24		2.05719	1.90382	0.08606	0.00174	0.00000
6653	5082	3637	647	23		2.16914	1.79325	0.19955	0.00265	0.00057
6192	5356	3970	446	13		2.13691	1.82989	0.16628	0.00197	0.00118
5895	5464	4549	169	14		2.10949	1.84956	0.13221	0.00255	0.00066
5949	5462	4423	188	20		2.04644	1.91313	0.07202	0.00142	0.00000
5812	5650	4491	136	19		2.03094	1.92893	0.06187	0.00153	0.00024
5972	5534	4535	149	20		2.02399	1.93639	0.05251	0.00240	0.00000
6022	5559	4559	139	18		2.01490	1.94974	0.05083	0.00192	0.00000
6129	5492	4213	290	19		2.05046	1.90475	0.08062	0.00152	0.00054

ms per formula unit						
Mn	Ca	Ti	Fe	Cr		#An
0.00077	0.98258	0.00066	0.01750	0.00000		0.93
0.00000	0.99590	0.00020	0.02090	0.00000		0.95
0.00082	0.95845	0.00105	0.02237	0.00000		0.91
0.00031	0.95082	0.00084	0.01885	0.00044		0.90
0.00055	0.86504	0.00042	0.01691	0.00000		0.82
0.00000	0.86985	0.00000	0.01846	0.00105		0.83
0.00060	0.88537	0.00035	0.01940	0.00008		0.85
0.00019	0.96123	0.00026	0.02045	0.00000		0.92
0.00077	1.00185	0.00000	0.01386	0.00067		0.95
0.00094	1.01137	0.00023	0.01214	0.00000		0.96
0.00070	0.96686	0.00000	0.01756	0.00000		0.92
0.00017	0.84876	0.00080	0.01861	0.00000		0.81
0.00041	0.87443	0.00079	0.01922	0.00000		0.84
0.00019	0.91524	0.00045	0.02135	0.00000		0.87
0.00000	0.97858	0.00020	0.02104	0.00000		0.93
0.00017	0.99173	0.00000	0.02023	0.00000		0.94
0.00037	1.00122	0.00009	0.01630	0.00048		0.95
0.00126	0.99633	0.00010	0.02047	0.00000		0.95
0.00143	0.97765	0.00064	0.01948	0.00000		0.92